Efficient spin transport through native oxides of nickel and permalloy with platinum and gold overlayers

B. L. Zink,[1,*] M. Manno,[2] L. O'Brien,[2,3] J. Lotze,[4] M. Weiler,[4] D. Bassett,[1] S. J. Mason,[1]
S. T. B. Goennenwein,[4,5,6] M. Johnson,[2] and C. Leighton[2]

[1]*Department of Physics and Astronomy, University of Denver, Denver, Colorado 80208, USA*
[2]*Department of Chemical Engineering and Materials Science, University of Minnesota, 421 Washington Avenue SE, Minneapolis, Minnesota 55455, USA*
[3]*Cavendish Laboratory, University of Cambridge, Cambridge, United Kingdom*
[4]*Walther-Meißner-Institut, Bayerische Akademie der Wissenschaften, 85748 Garching, Germany*
[5]*Physik-Department, Technische Universität München, 85748 Garching, Germany*
[6]*Nanosystems Initiative Munich (NIM), Schellingstraße 4, 80799 München, Germany*

(Received 21 July 2015; revised manuscript received 23 March 2016; published 2 May 2016)

We present measurements of spin pumping detected by the inverse spin Hall effect voltage and ferromagnetic resonance spectroscopy in a series of metallic ferromagnet/normal metal thin film stacks. We compare heterostructures grown *in situ* to those where either a magnetic or nonmagnetic oxide is introduced between the two metals. The heterostructures, either nickel with a platinum overlayer (Ni/Pt) or the nickel-iron alloy permalloy (Py) with a gold overlayer (Py/Au), were also characterized in detail using grazing-incidence x-ray reflectivity, Auger electron spectroscopy, and both SQUID and alternating-gradient magnetometry. We verify the presence of oxide layers, characterize layer thickness, composition, and roughness, and probe saturation magnetization, coercivity, and anisotropy. The results show that while the presence of a nonmagnetic oxide at the interface suppresses spin transport from the ferromagnet to the nonmagnetic metal, a thin magnetic oxide (here the native oxide formed on both Py and Ni) somewhat *enhances* the product of the spin-mixing conductance and the spin Hall angle. We also observe clear evidence of an out-of-plane component of magnetic anisotropy in Ni/Pt samples that is enhanced in the presence of the native oxide, resulting in perpendicular exchange bias. Finally, the dc inverse spin Hall voltages generated at ferromagnetic resonance in our Py/Au samples are large, and suggest values for the spin Hall angle in gold of $0.04 < \alpha_{SH} < 0.22$, in line with the highest values reported for Au. This is interpreted as resulting from Fe impurities. We present indirect evidence that the Au films described here indeed have significant impurity levels.

DOI: 10.1103/PhysRevB.93.184401

I. INTRODUCTION

A nonmagnetic (NM) metal in proximity to a ferromagnet (FM) causes an additional magnetization damping in the FM. The excess angular momentum from the FM flows into the NM, where it forms a diffusive pure spin current in a process known as spin pumping [1–3]. In materials with strong spin-orbit coupling (SOC) this spin current drives a measurable dc voltage, V_{ISH}, as a result of the inverse spin Hall effect (ISHE) [4–6], such that V_{ISH} can be taken as an electrical measure of the ability of the FM/NM hybrid to generate pure spin current [7,8]. Spin-pumping experiments, either detected as a modification in magnetization damping or via V_{ISH}, have become ubiquitous and essential for studies in nanomagnetism, spintronics, and spincaloritronics [9–11]. One way to frame the usual picture of spin pumping, which has been explained via a complete quantum mechanical theory [2,3], is that some fraction of the spin-polarized electrons in a FM incident on an interface with a NM will experience spin-flip scattering. The required change in angular momentum between the incoming and outgoing electron wave functions at the interface drives a pure spin current into the NM. As commonly noted, this is the inverse scattering process to spin-transfer torque [12] where a spin-polarized current in a NM exerts a torque on a FM layer. The theories of both effects rely on the existence of electron wave functions on both sides of a clean interface between FM and NM. The spin-pumping theory has a logical extension to the interface between an insulating FM (FMI) and a nonmagnetic metal, where the spin excitation in the FMI is carried by magnons which couple to the NM electron wave function at the FMI/NM interface [13–16].

The theoretical requirement for well-defined electron wave functions has motivated experimentalists to focus on well-controlled interfaces in studies of the spin-pumping efficiency of FM/NM interfaces [11], and a wide range of studies have confirmed that spin pumping is strongly reduced by the presence of nonmagnetic insulators or damage at interfaces [17–20]. Very recently, however, two groups [21,22] have surprisingly shown that inserting the *antiferromagnetic* oxide NiO, even in the thickness regime without well-defined bulk magnetic order at the relevant measurement temperature, does not stop transport of spin current between the ferrimagnetic insulator yttrium iron garnet (YIG) and Pt. This has been attributed to either antiferromagnetic (AF) magnons or AF spin fluctuations, although more work needs to be done to fully clarify the mechanisms. In particular, the suppression of the AF ordering temperature with reduced thickness is an important factor, as it will dictate whether long-range AF order or only short-range AF spin fluctuations are present at the measurement temperature. A recent theory also predicts spin pumping from an antiferromagnet with well-defined

*barry.zink@du.edu

long-range order with expected voltages on the order of that seen for ferromagnets [23]. Furthermore, a study of spin pumping performed above the T_c of a FM film also showed ISHE dc voltages in the regime where only FM correlations are present [24]. All of these very recent results question the typical view of the requirements for spin transport across an interface in response to magnetization dynamics. In this paper we examine this spin transport by intentionally oxidizing the surface of transition-metal FM thin films. Such native oxide layers have been largely avoided by the spintronics and spincaloritronics communities up to this point, due to the expectation that clean electronic interfaces will lead to the most effective spin transport and the largest spin-pumping effects. Surprisingly, we show the opposite, i.e., that the magnetic native oxides of Ni and Py somewhat enhance the efficiency of spin transport across the interface and/or subsequent electrical detection of spin current via the ISHE.

In electrically detected spin pumping experiments, the electrical detection of the pumped spin current is enabled by the inverse spin Hall effect, so that one inherently probes both the NM's efficiency of converting charge to spin current, and the ability of the interface to transmit spin current from the precessing magnetization in the FM to the NM. Spin current conversion by the ISHE is usually quantified by the spin Hall angle [8]

$$\alpha_{\mathrm{SH}} = \frac{\sigma_{xy}^{s}}{\sigma_{xx}^{c}} \frac{e}{\hbar}, \tag{1}$$

where σ_{xx}^{c} and σ_{xy}^{s} denote longitudinal charge and transverse spin conductivities, respectively. The interface is normally discussed in terms of a spin-mixing conductance $g_{\uparrow\downarrow}$, which is ultimately related to the spin-dependent transmission probabilities at the interface [25]. As shown below (Sec. V A), electrically detected spin pumping cannot separately determine these quantities, and the most precise description of our results is in terms of an overall electrically detected spin pumping efficiency, $g_{\uparrow\downarrow,\mathrm{eff}}\alpha_{\mathrm{SH}}$. In the fairly common limit of the normal-metal thickness, t_{N}, much greater than the spin diffusion length, λ_{sd}, in the normal metal, λ_{sd} can also not be separately determined by electrically detected spin pumping experiments, which only allow extraction of the product $g_{\uparrow\downarrow,\mathrm{eff}}\alpha_{\mathrm{SH}}\lambda_{\mathrm{sd}}$. Due to this interrelation and the difficulty of the measurements themselves, there is currently considerable disagreement regarding the size of α_{SH} and λ_{sd} in various materials [7,8].

Our results include not only electrically detected spin pumping in cavity-based ferromagnetic resonance (FMR), but also broadband FMR spectroscopy, structural characterization by x-ray reflectivity and Auger-electron spectroscopy, and SQUID and alternating gradient field magnetometry (AGFM). We also clearly demonstrate the presence of out-of-plane magnetic anisotropy at Ni/Pt interfaces. Interestingly, this out-of-plane anisotropy grows substantially when NiO is added between the FM and large spin-orbit coupling (SOC) material Pt, leading to a perpendicular exchange bias in this sample [26,27]. The increased anisotropy, which persists far above the blocking temperature, suggests that the SOC film enhances the exchange anisotropy of the underlying layers. Finally, electrically detected spin pumping in a series of Py/Au heterostructures proves that the Py/Au and Py/PyOx/Au interfaces both show large spin-pumping efficiency $g_{\uparrow\downarrow,\mathrm{eff}}\alpha_{\mathrm{SH}}$, suggesting values for the spin Hall angle of Au in line with the largest values found in the literature [28–30]. We provide strong, if indirect, evidence that this increase in α_{SH} is caused by increased scattering from magnetic impurities in the Au films, as suggested by theoretical predictions [31].

II. EXPERIMENT

FM/NM bilayers with various interfaces were grown either by sputtering in high vacuum (HV) or e-beam evaporation in ultrahigh vacuum (UHV) on Si-N coated Si substrates. Three Ni heterostructures with Pt overlayers were prepared via dc sputtering in 3×10^{-3} Torr of Ar after pumping to a base pressure of 2×10^{-6} Torr or better. Approximate sputter rates were 0.06–0.09 nm/s at dc powers of 100–125 W, dependent on material. One stack was grown without breaking vacuum between Ni and Pt depositions and with minimal time between depositions (referred to as Ni/Pt). Another was removed from vacuum after Ni deposition for approximately 24 hours and stored in a clean, humidity-controlled environment before reloading in the sputtering system for Pt deposition (referred to as Ni/NiO/Pt). This elapsed time is more than enough to form a complete native Ni oxide layer, which we presume to be NiO, an oxide that is antiferromagnetic *in bulk* with a Néel temperature $T_N = 525$ K [32]. Growth of native NiO on Ni thin films is known to result in a thickness-dependent antiferromagnetic blocking temperature [33] and substantial nonuniformity in thickness, however, so that we expect relatively poor isolation between Ni and Pt layers. A final Ni heterostructure was also grown entirely *in situ*, but with the addition of a Ag layer between the Ni and Pt (referred to as Ni/Ag/Pt).

Three Py heterostructures with Au NM overlayers were prepared via e-beam evaporation in UHV using a single Py crucible from source material with nominal composition $Ni_{80}Fe_{15}Mo_5$. The resulting Py film composition, determined from energy-dispersive x-ray spectroscopy analysis (EDS) in a scanning electron microscope for all Py films is approximately 85% Ni and 15% Fe, with no evidence of Mo incorporation. Film stacks were deposited after reaching a base pressure of 5×10^{-9} Torr or better at rates of ∼0.1 nm/s. One stack was again grown without breaking vacuum (Py/Au), with a second film removed from the UHV chamber and exposed to atmosphere in the vented load lock for ∼24 hours before reintroduction to vacuum and deposition of Au (Py/PyOx/Au). Permalloy's native oxide is not simple, as will be discussed in more detail below, although it is also expected to have significant nonuniformity in thickness. A final Py heterostructure was first capped with (nominally) 2–3 nm of Al, then allowed again to oxidize for 24 hours before Au deposition (Py/AlOx/Au). Multiple 1 cm × 1 cm substrates were used in each deposition and pieces from each were used for structural, magnetic, and dynamic characterization.

The individual layer and total thickness and chemical depth profile of each heterostructure was probed via grazing-incidence x-ray reflectivity (GIXR) using Cu K_α radiation. The chemical depth profile was also probed using Auger electron spectroscopy and ion-beam sputtering, to provide

complementary information. Depth profiles reported below used the following Auger lines, listed with the element, peak energy, and the common symbol: C, 263 eV, KLL; N, 375 eV, KLL; O, 503 eV, KLL; Si, 1614 eV, KLL; Fe, 595 eV, LMM; Ni, 844 eV, LMM; Ag, 349 eV, MNN; Pt, 1960 eV, MNN; Au, 2015 eV, MNN. For these samples it was not possible to quantitatively calibrate the correction factors that take Auger detector sensitivity and cross section into account beyond the level of a 5%–10% error in absolute composition, so the most meaningful information from Auger electron spectroscopy comes from *relative* values for a given element as a function of depth.

The inverse spin Hall voltage, V_{ISH}, was measured using a magnetic resonance spectrometer on 1 mm × 5 mm pieces cut from the larger substrates using an automated diamond-blade wafer saw. Wire bonds connected to the ends of the long axis allow measurement of the dc voltage generated in response to FM resonance in a 9.85 GHz microwave field. The sample was placed as near as possible to a node of the electric field and antinode of the magnetic field in a TE_{102} cavity and H applied in the plane of the samples was swept to map both the resonance and ISHE voltage response.

We performed FMR spectroscopy on unpatterned bi- and trilayer samples coated with ∼1 μm of photoresist and placed face down on a low-loss coplanar stripline broadband 50 Ω waveguide with 150 μm center conductor width. The static field H_0 was applied perpendicular to the plane of the sample (out-of-plane) to avoid contributions from 2-magnon scattering. A vector network analyzer measured transmission, S_{21}, as a function of frequency from 10–30 GHz and applied field. Details of the analysis are presented in Sec. III C.

Magnetometry was performed both in commercial dc SQUID and alternating gradient field magnetometers. SQUID M vs H measurements at fields up to 1 T provided accurate values of saturation magnetization, while AGFM provided detailed characterization of switching behavior at small fields applied both in the plane and perpendicular to the plane. In both SQUID and AGFM scans the linear background due to the diamagnetic response of the Si/Si-N substrate was subtracted. The total moment of the heterostructures was on the order of 1×10^{-4} emu (1×10^{-7} Am^2) or larger. Sample thickness measured by GIXR and sample area measured using a micrometer provided the sample volume in order to convert total moment to magnetization.

III. RESULTS

A. GIXR and Auger depth profiling

Figure 1 compares x-ray reflectivity vs scattering wave vector, $q_z = 4\pi \sin(2\theta)/\lambda$ with $\lambda = 1.5418$ Å for Cu K_α excitation, for all six samples. Ni heterostructures appear in Fig. 1(a) and Py heterostructures in Fig. 1(b). Ni/Pt and Py/Au samples in the respective panels are as-measured reflectivity, with subsequent data sets in each panel offset upwards by two decades. Some important details of the bi- or trilayer sample structures are obvious even by inspection from these plots. First, the Ni/Pt stack shows Kiessig fringes due to both layers, as expected, since the Pt and Ni have quite different density. Significantly, the addition of an extra layer in the

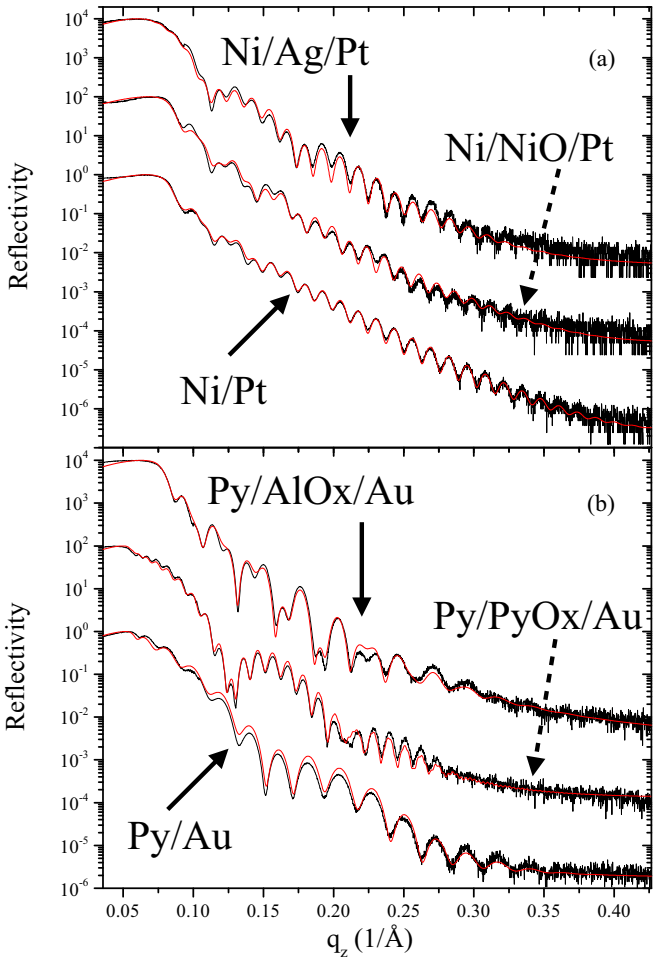

FIG. 1. X-ray reflectivity vs q_z for (a) Ni/Pt, Ni/NiO/Pt, Ni/Ag/Pt and (b) Py/Au, Py/PyOx/Au, and Py/AlOx/Au samples. Black lines represent measured data with red lines the result of refinement to the model density profiles shown in Figs. 2 and 3. The top two plots in each panel are offset upward by a factor of 100 and 10 000.

Ni/NiO/Pt sample, caused by the oxidization of the Ni film, introduces noticeable additional modulation at low q_z that is not present in Ni/Pt. Similar effects are seen upon addition of the Ag interlayer. All three Py-based samples are also visibly different, with well-defined modulation minima in the Py/PyOx/Au curve near $q_z = 0.13$ and 0.2 Å^{-1} that are absent in the Py/Au case. These minima indicate the separation of the Py and Au layers by a relatively low x-ray scattering length density (SLD) layer (see below). As expected, the insertion of an Al-O layer between the Py and Au results in multiple visible periods.

SLD vs depth profiles derived from quantitative refinement are compared directly to Auger electron spectroscopic (AES) depth profiles for all six heterostructures in Figs. 2 and 3. Labels in the top panels for each film stack give the GIXR refinement results for thickness t, Gaussian roughness of the top surface σ, and density ρ for each of the film components. Each refinement included the bulk Si substrate and a ∼200 nm thick Si-N layer with density 3.0 ± 0.2 g/cm^3 and surface roughness $\sigma \approx 0.7$ nm. Auger spectra were collected as a

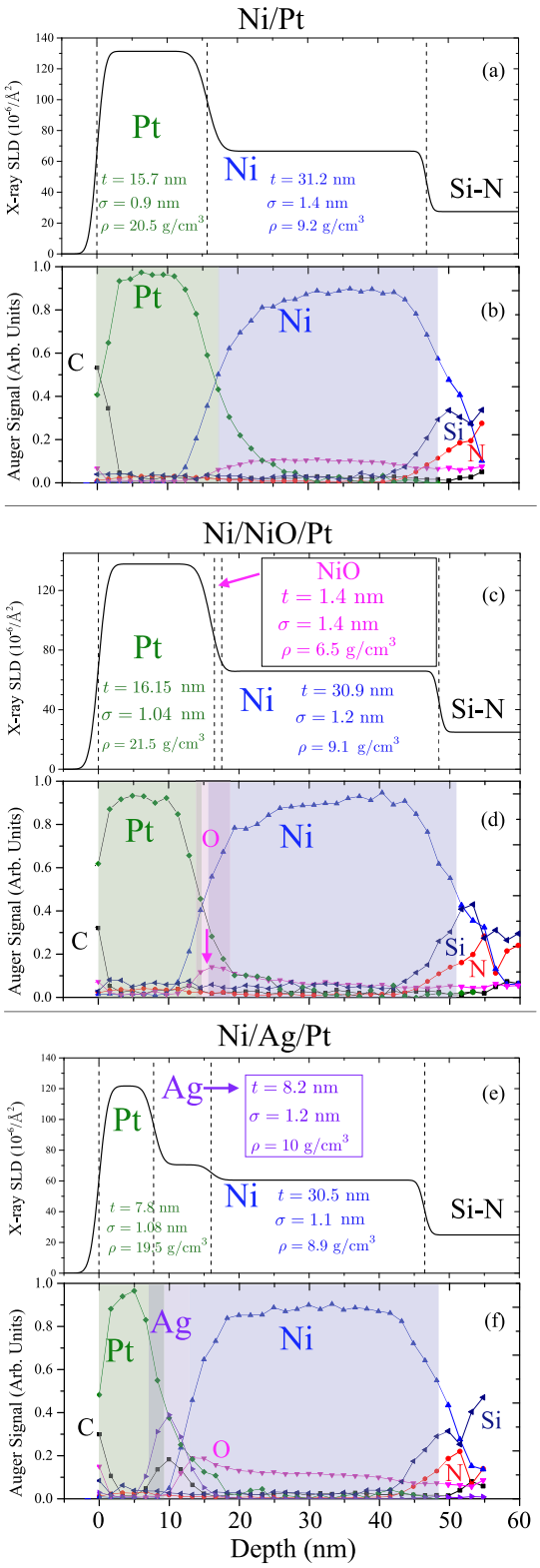

FIG. 2. Refined x-ray scattering-length density (SLD) and depth-profiled Auger electron spectroscopy for (a)–(b) Ni/Pt, (c)–(d) Ni/NiO/Pt, (e)–(f) Ni/Ag/Pt heterostructures. Ni films left exposed to atmosphere for ∼24 hours between FM and NM layer deposition show clear accumulation of O Auger electron signal localized to the interface.

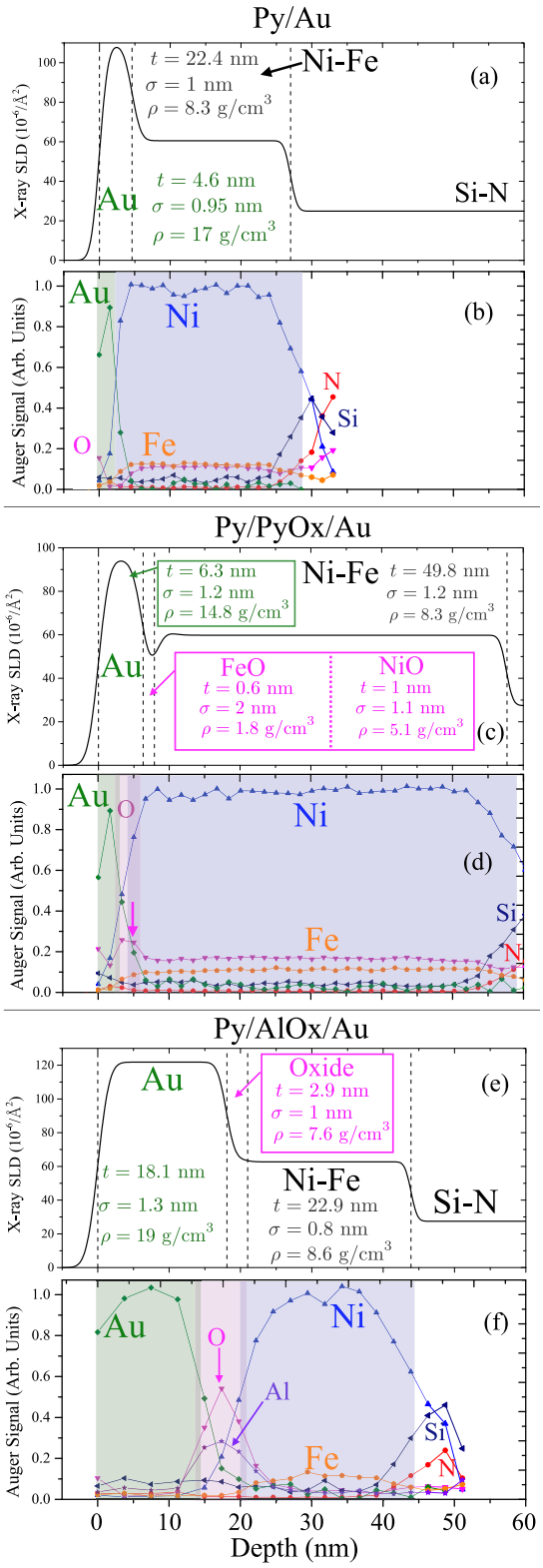

FIG. 3. Refined x-ray scattering-length density (SLD) and depth-profiled Auger electron spectroscopy for (a)–(b) Py/Au, (c)–(d) Py/PyOx/Au, (e)–(f) Py/AlOx/Au heterostructures. Py layers left exposed to atmosphere for ∼24 hours between FM and NM layer deposition show clear accumulation of O Auger electron signal localized to the interface.

function of total 4 keV sputtering time, which was converted to approximate etching depth using the total sample thickness as determined from GIXR. We assumed a constant etch rate throughout material layers for all heterostructures, with the exception of the Py/AlOx/Au, where the much thicker Au layer, which has an approximately 20% slower sputter etch rate than other species, required scaling of the rate-to-depth conversion in the Au-dominated portion of the depth profile. Auger depth profiles in all films show an interface width of approximately 10 nm. These apparently broad interfaces are expected due to the polycrystalline nature of the films and resulting nonuniform milling. We clarify that these overlapping lines in Auger spectra *cannot* be interpreted as evidence of excessive interdiffusion of the adjacent layers, as even a perfectly sharp interface between two polycrystalline films would show this ∼10 nm apparent interface width in part due to preferential sputtering at the grain boundaries. The colored boxes in each AES profile are placed at the half-maximum of the elemental peaks and in all samples correlate well with the GIXR depth profile.

The SLD profile for the Ni/Pt sample in Fig. 2(a) shows no evidence of an oxide layer at the interface, and values of density reduced somewhat from bulk ρ as expected in polycrystalline films; this is a pattern in ρ seen for all metals throughout all heterostructures. The corresponding AES profile in Fig. 2(b) shows a clean interface between Pt and Ni, although a small oxygen signal is present throughout the depth of the Ni film. In the intentionally oxidized film, in contrast, the AES profile [Fig. 2(d)] shows a clear accumulation of O at the interface in addition to the O background in the film [34], and GIXR refinement [Fig. 2(c)] reveals a thin NiO layer that is likely not continuous since $\sigma \approx t$ for this layer. However, detection of this layer in both GIXR [easily seen in Fig. 1(a)] and AES indicates that at least a significant area of the interface was oxidized during the 24 hour exposure to atmosphere. Finally, the Ni/Ag/Pt sample [Figs. 2(e)–2(f)] shows the expected Ag layer at the interface, but AES also shows small oxygen and carbon peaks at the interface in addition to the O background again through the Ni film. The C and O peaks suggest that the addition of Ag causes the Ag/Pt top layer to prevent oxidation of the interface poorly in comparison to the Pt layer alone. This occurs due to the high interfacial energy of thin Ag layers on many surfaces, leading to increased roughness and likely formation of pinholes in subsequent capping layers that allow both O and C from atmospheric gases and contaminants to diffuse to the reactive Ni surface. Diffusion of O even through much thicker Ag layers (80 nm) and subsequent oxidization of a transition-metal FM surface has been shown very clearly in previous work on nonlocal spin valves [35]. The AES profile in Fig. 2(f) suggests that even a subsequent capping with 7.8 nm of Pt does not entirely prevent O diffusion and oxidation of the underlying Ni. This will most likely lead to a Ag layer with higher electrical resistivity than for clean bulk Ag, although this value is not needed in any subsequent analysis.

As seen for the Ni series, the intentionally "clean" interface Py/Au heterostructure shows evidence of an oxide layer in neither SLD [Fig. 3(a)] nor AES profiles [Fig. 3(b)]. Here a small O signal is again detected in the bulk of the Py film for the Py/Au and Py/PyOx/Au heterostructures. We believe this was introduced via a small leak in the UHV chamber that was repaired before growth of the Py/AlOx/Au heterostructure. The intentionally oxidized Py/PyOx/Au sample shows clear evidence of the oxidized interface in both GIXR and AES profiles [Figs. 3(c)–3(d)]. The native oxide of the Fe-Ni alloy is significantly more complicated than the elemental Ni film, but has been studied in detail by neutron and x-ray reflectivity [36]. That work showed a two-layer oxide with FeO and NiO components that form at different rates at various oxidation temperatures. To reach a satisfactory refinement of GIXR for this film stack we introduced this two-layer oxide, and both layers again are thin and show high roughness suggesting a potentially discontinuous but high-surface-area coverage oxide at the interface. Finally, the Py/AlOx/Au, where we inserted the non-native, nonmagnetic Al oxide by 24 hour room-temperature oxidation of a 2–3 nm Al layer, again shows clear evidence of both O and Al peaks in the AES profile [Fig. 3(f)]. However, for this sample, refinement of GIXR gives very similar results with and without an interfacial oxide layer, and the resulting ρ for the oxide is more than 2× higher than the bulk value for the expected Al_2O_3 layer. Our interpretation is that there is clearly an interfacial oxide, but one that is likely a mix of a very thin Al_2O_3 component with regions of an oxide of Ni, Fe, or a mix of all three metal ions. This accounts for the apparent anomalously high SLD in this region. We note, however, that the total thickness of the oxide layer is significantly greater than the roughness, and regions of direct contact between the metallic Py and Au layers should be largely eliminated.

B. V_{ISH} via electrically detected spin pumping

Results of inverse spin Hall effect measurements via cavity FMR driven electrically detected spin pumping are shown in Fig. 4. In each heterostructure, the FMR resonance at $\nu_{MW} = 9.85$ GHz with static field $\vec{H}_0$ applied along $\pm\hat{x}$ ($\theta = 0$ or 180°) and h_{MW} applied in the $\hat{y}$ direction generates a Lorentzian dc voltage response. This is measured, as shown schematically at lower left, with two contacts along the $\hat{y}$ direction. As expected, reversing the static applied field ($\theta = 180^\circ$) flips the sign of the dc voltage. The peak height, resonance width, and resonance field used in quantitative analysis (shown in Table I) are all determined from the data using Lorentzian fits to the full response. Note that the samples were each carefully positioned in the cavity in an antinode of the magnetic field, resulting in V_{ISH} signal with dominantly symmetric Lorentzian line shape.

Figures 4(a)–4(c) show the results for the Ni heterostructure series. Recall that GIXR and AES confirm that, apart from the presence of NiO, the Ni/Pt and Ni/NiO/Pt samples are very similar, with both t_F and t_N approximately equal. In electrically detected spin pumping, simple comparisons of peak V_{dc} must be treated with caution since the Gilbert damping α (see Sec. III C below) and thus the degree of magnetization excitation, as well as the electrical resistance of the layer stacks, vary somewhat across the series. We take these effects into account in the quantitative analysis described below (Sec. V). However as a first estimate, the trend in V_{dc} does suggest that the overall efficiency of spin pumping is approximately 3× *larger* for the sample with the NiO layer compared to Ni/Pt alone. Recall that although the ordering temperature of NiO is very high *in bulk*, these room temperature measurements occur well

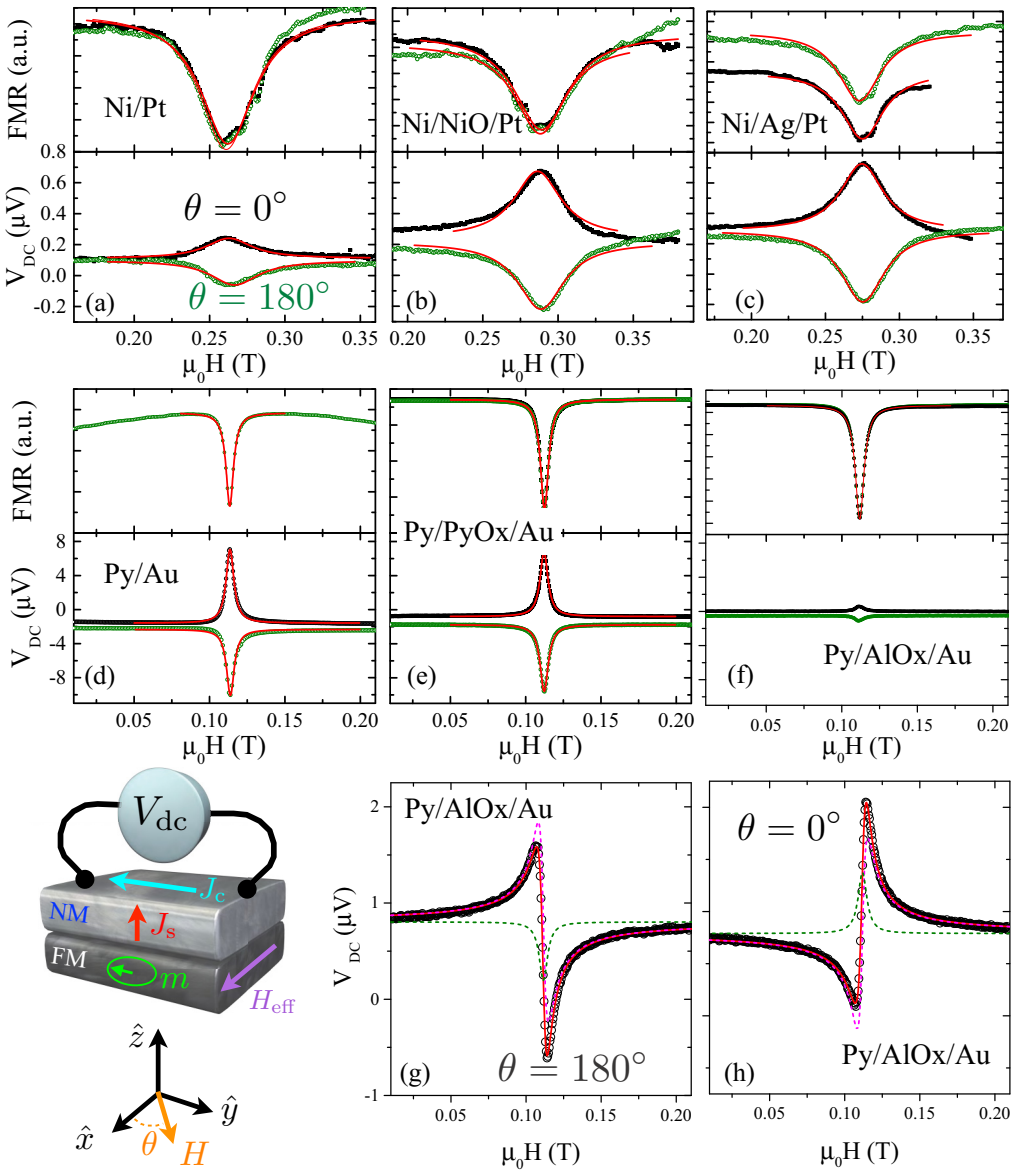

FIG. 4. Inverse spin Hall effect measurements via spin pumping excited by cavity FMR. Top plots of panels (a)–(f) show the FMR response as a function of field with 9.85 GHz microwave excitation. Bottom plots show the dc spin-pumping voltage measured on the NM layer as a function of field. (a) Ni/Pt, (b) Ni/NiO/Pt, (c) Ni/Ag/Pt, (d) Py/Au, (e) Py/PyOx/Au, (f) Py/AlOx/Au. Note that the presence of the native oxide in both series slightly increases the total ΔV_{ISH} (see text), and that the Py/Au series generates large ΔV. For only the Py/AlOx/Au, the film stack could not be placed exactly at the node of the electric field, and V_{dc} is dominated by a rectification-driven asymmetric (peak-dip) component. Panel (f) shows the spin-pumping component extracted by fit from the raw signals shown in (g) and (h). In (g) and (h) symbols are measured V_{dc}, solid red lines the fit, and dashed lines show the separate symmetric and antisymmetric components.

above the expected antiferromagnetic blocking temperature in this very thin (<2 nm) NiO layer. A second Ni/Pt piece was also measured (not shown) and confirms the low signal compared to Ni/NiO/Pt. A similar enhancement appears in Ni/Ag/Pt [Fig. 4(c)]. This is a nearly equally surprising result, since prevailing wisdom suggests that inserting a thin layer of metal such as Ag with relatively low SOC and long spin-diffusion length (typically reported to be 130–150 nm at room temperature [37], so that $\lambda_{sd} > 10 \times t_{Ag}$) should have little effect on spin transport. The Ag layer is rather expected to result in an electrical shunting of the ISHE voltage (since its electrical conductivity is typically higher than that of Pt); thus the introduction of a Ag layer is expected to reduce the measured dc voltage.

Figures 4(d)–4(f) show the results for the Py heterostructures. Here the $\theta = 180^\circ$ curves have been shifted by 1 μV from the $\theta = 0$ curves for clarity, and the Py/PyOx/Au signals were shifted by 2 μV to plot all Py samples on the same y axis. A similar comparison of V_{dc} can be made between the Py/Au and Py/PyO/Au samples shown in Figs. 4(d) and 4(e), although the wider variance in t_F must be taken into account. Although the two heterostructures have very similar t_N, the Py/PyOx/Au stack has $t_F \approx 2\times$ thicker than the Py/Au stack. As a result (see Table I) the bulk of the FM layer shunts the

TABLE I. Sample parameters relevant for determining precession cone angle and spin-pumping (SP) efficiency. t_x: thickness of layer x, R_{sp}: resistance between V_{dc} leads in SP geometry, ℓ_{sp}: distance between V_{dc} leads in SP geometry, $\mu_0 H_{res}$: resonance field in SP geometry, ΔH: FWHM resonance linewidth in SP, h_y: driving field in SP, g: g factor from FMR, α: damping parameter from FMR, M_{eff}: effective M from FMR, $\mu_0 \Delta H_0$: inhomogeneous broadening from broadband FMR, $\mu_0 H_{calc}$: FMR resonance calculated for 9.85 GHz from Kittel equation using g and M_{eff} from broadband FMR, M_s: saturation magnetization measured via SQUID, H_k: anisotropy field from FMR and SQUID, $|m_y| \cdot |m_z|/M_s^2$: calculated precession cone angle for SP geometry, $\sin^2 \Theta_{est}$: typical estimation of precession cone angle in SP (for ellipticity correction $P = 1$).

	Ni/Pt	Ni/NiOx/Pt	Ni/Ag/Pt	Py/Au	Py/PyOx/Au	Py/AlOx/Au
t_F (nm)	31.2	30.9	30.5	22.4	49.8	22.9
t_{Ox} (nm)		1.4			1.6	2.9
t_{Ag} (nm)			8.2			
t_N (nm)	15.7	16.5	7.8	4.9	6.3	18.1
R_{sp} (Ω)	35/33	31	35	46	25	14
ℓ_{sp} (mm)	4.8	5.1	4.8	4.4	4.4	4.5
$\mu_0 H_{res}$ (T)	0.263	0.286	0.274	0.1136	0.1123	0.112
$\mu_0 \Delta H$ (mT)	36.53	35.4	39.8	6.26	7.09	4.1
$\mu_0 h_y$ (mT)	0.032	0.032	0.032	0.032	0.032	0.054
g	2.19894(47)	2.19634(38)	2.1980(13)	2.11056(38)	2.1015(11)	2.10802(28)
α	0.02816(45)	0.03000(23)	0.02918(51)	0.00831(8)	0.00799(9)	0.00774(12)
M_{eff} (kA/m)	163.62(10)	793.77(87)	104.68(25)	686.99(11)	699.09(31)	680.048(73)
$\mu_0 \Delta H_0$ (mT)	2.60(56)	0.58(29)	4.41(53)	0.34(13)	1.17(14)	2.33(17)
$\mu_0 H_{calc}$ (T)	0.232	0.273	0.260	0.113	0.112	0.114
M_s (kA/m)	357.3(1.5)	376(12)	236.6(2.3)	653(4)	582(3)	506(3)
H_k (kA/m)	193.7	296.9	131.9	−34	−117	−174.2
$\lvert m_y\rvert \cdot \lvert m_z\rvert/M_s^2$	3.951×10^{-6}	3.185×10^{-6}	3.48×10^{-6}	3.673×10^{-5}	3.915×10^{-5}	1.209×10^{-4}
$\sin^2 \Theta_{est}$	1.023×10^{-6}	1.09×10^{-6}	8.619×10^{-7}	3.484×10^{-5}	2.716×10^{-5}	2.353×10^{-5}

generated V_{dc}. This means that the roughly equal V_{dc} values between these samples suggest a similarly large enhancement in spin-pumping efficiency when the PyOx is inserted between Py and Au. As noted for the Ni heterostructures, all data in Fig. 4 were taken at room temperature, much higher than the temperature where magnetic order is normally believed to occur in oxidized permalloy of this thickness [38–40]. We address these issues in much more detail below (Sec. IV A). Note also that the spin-pumping response is large, despite the use of Au as the NM layer. This indicates qualitatively that our Au films show larger values of α_{SH} than many reports [10,41–46], as will be shown quantitatively below (Sec. V A).

When an aluminum oxide layer was added between Py and Au, the signal is strongly reduced. For *only* this sample, we were not able to completely remove a component of V_{dc} from rectification, because the sample could not be placed perfectly at the electric field node of the cavity. As a result, the total voltage, shown in Figs. 4(g) and 4(h), is a superposition of a peak-dip response with a small Lorentzian. The total response is itself much less than the peaks in the other two Py samples ($\sim 2\ \mu$V vs $\sim 8\mu$V). We assume that the inverse spin Hall effect voltage yields a purely Lorentzian line shape, while any rectification signal exhibits antisymmetric line shape. This allows us to extract the spin-pumping portion of the response for this sample for $\theta = 180°$ and $\theta = 0°$ with $H_0 > 0$ by fitting the total voltage to [47]

$$V_{dc} = L\frac{\Delta H^2}{(H - H_0)^2 + \Delta H^2} + D\frac{\Delta H(H - H_0)}{(H - H_0)^2 + \Delta H^2}. \quad (2)$$

Here L and D are the magnitudes of the spin-pumping and spin-rectification components, respectively, ΔH is the linewidth, H_0 is the resonance field, and H the applied field. Fits to the total response, along with the separate components of the signal, are shown for $\theta = 0$ [Fig. 4(h)] and $\theta = 180°$ [Fig. 4(g)] peaks. The lower panel in Fig. 4(f) shows only the spin-pumping component obtained by subtracting the rectification signal from the measured response. Quantitative determination and comparison of spin-pumping efficiency across these samples, using parameters determined from FMR spectroscopy and magnetometry, is described in Sec. V A below.

C. Broadband FMR spectroscopy and damping

To best understand the dynamic response of these FM/NM samples and confirm the origin of the enhanced V_{dc} as spin pumping, we performed broadband FMR spectroscopy as a function of field and frequency at room temperature. Figures 5(a) and 5(b) show example raw real and imaginary parts of the microwave transmission S_{21} of the FM-loaded coplanar waveguide, respectively, for two samples at $\nu_{MW} = 20$ GHz. All samples but two showed single-peak spectra of this type. The spectra were fitted using a technique described in detail elsewhere [48,49] to find the resonance field, H_{res}, and linewidth, ΔH. A fit of H_{res} vs f to the Kittel equation in the out-of-plane geometry,

$$H_{res} = \frac{2\pi f}{|\gamma|\mu_0} + M_{eff} \quad (3)$$

with $\gamma = g\mu_B/\hbar$, as shown in Fig. 5(c), gives the g value g and $M_{eff} = M_s - H_k$. The measured saturation magnetization M_s

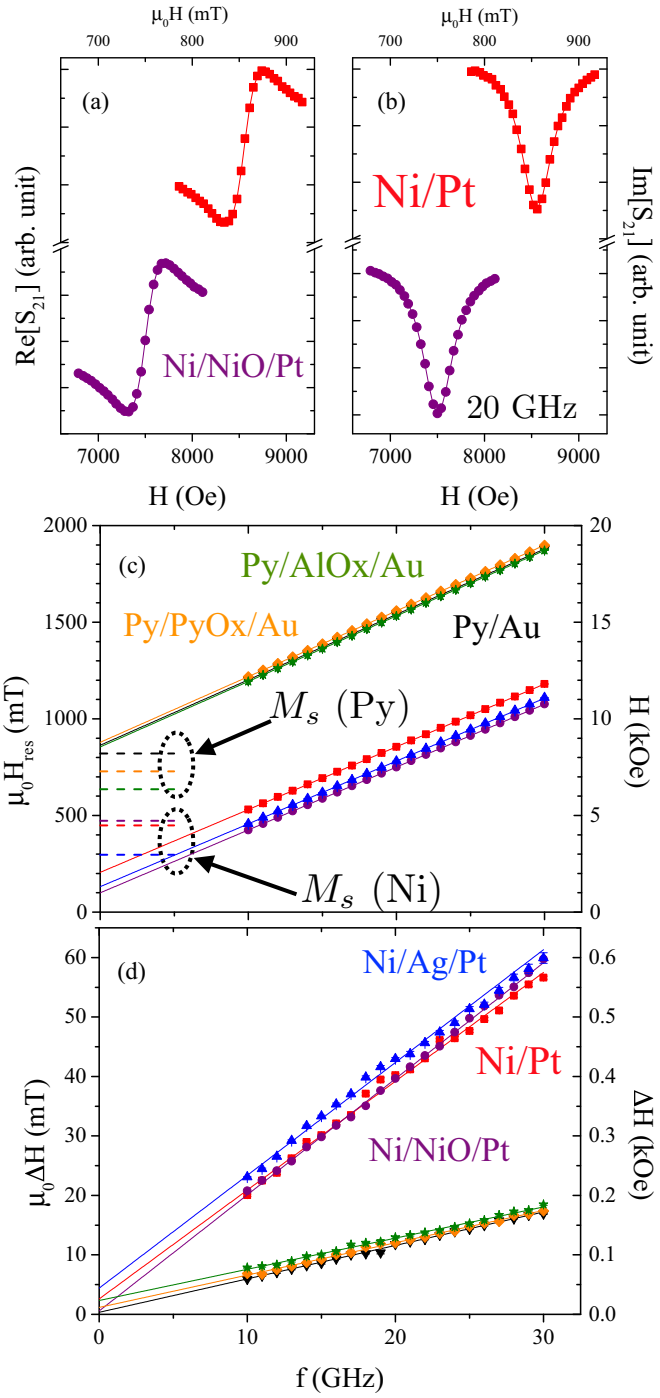

FIG. 5. FMR data for Ni- and Py-based samples. Example raw FMR response for Ni/Pt and Ni/NiO/Pt samples shown as (a) real and (b) imaginary parts of S_{21} at 20 GHz. The fits shown determine $H_{\rm res}$ and ΔH for each f as shown in (c) and (d) for all samples. Lines in (c) are fits to the out-of-plane Kittel equation [Eq. (3)] and those in (d) are linear fits [Eq. (4)] to extract α.

for each sample is indicated by the dashed lines in Fig. 5(c). This clearly shows that Ni samples, with intercept $M_{\rm eff} < M_s$, all show relatively large positive anisotropy field H_k indicating an out-of-plane anisotropy, while Py samples, with $M_{\rm eff} > M_s$, show slightly negative H_k indicating in-plane anisotropy. Fits of ΔH vs f in Fig. 5(d) to

$$\Delta H = \frac{4\pi\alpha f}{|\gamma|\mu_0} + \Delta H_0 \tag{4}$$

give the Gilbert damping parameter, α, and the inhomogeneous linewidth broadening, ΔH_0.

The Ni/Ag/Pt and Py/PyO/Au samples, two of the samples with the thickest FM layers studied, did each show a second, smaller peak for some portion of the range of frequencies measured. This peak was separated by at least 50 mT (500 Oe) from the main resonance, and in the case of Ni/Ag/Pt we were able to separately fit and track the two peaks. This sample showed nearly identical slope of the line fit to $H_{\rm res}$ vs f, indicating the same g value as the main peak with a frequency-independent shift in field, and a slightly higher value of α indicated by a larger slope of ΔH vs f and approximately 4 mT higher inhomogeneous broadening. If these features shift in frequency and become coincident in the *in-plane* magnetic field geometry used for electrically detected spin pumping, this second peak could help explain the larger-than-expected $V_{\rm dc}$ values. Note, however, that only a single peak was found in the Py/Au and in the Ni/NiO/Pt. The surprisingly large $V_{\rm ISH}$ and $g_{\uparrow\downarrow}\alpha_{sh}$ values found in these samples apparently have no easy explanation in this second resonance.

D. Magnetometry and anisotropy

Figure 6 shows M vs H for the Ni film series and clarifies the role of out-of-plane magnetic anisotropies. Each panel shows M measured for both H applied in the plane (blue) and out of the plane of the film (red). Dashed lines indicate $\pm\mu_0 M_{\rm eff}$ from the FMR measurements. The M_s values are somewhat reduced from literature values of bulk Ni (M_s = 490 emu/cm^3 = 490 × 10^3 A/m), which could be related to the inclusion of O in the films as shown in Fig. 2 [50]. The top graph shows that Ni/Pt maintains a well-defined in-plane easy axis, although reduced remanence ($M_r \sim 0.6 M_s$) and low out-of-plane saturation field $H_{\rm sat}$ compared to the expected value (near $\mu_0 H = \mu_0 M_s = 450$ mT) clearly indicates the presence of a mixed magnetic anisotropy with some out-of-plane component. The addition of the Ag layer increases this anisotropy (seen in further reduced in-plane M_r and $H_{\rm sat}$). The presence of the NiO has the most dramatic effect, however, with strongly reduced in-plane M_r and $H_{\rm sat}$ and the opening of obvious hysteresis in the out-of-plane loop, confirming an out-of-plane anisotropy. Note in each panel that $M_{\rm eff}$ taken from FMR gives general agreement (with slight underestimation) with the measured reversal. The overall picture is entirely consistent with the pattern of $M_{\rm eff}$ and H_k seen in the Ni films in FMR. It is also clear from Fig. 6 that a similar trend appears in the in-plane coercive field, $H_{c,\parallel}$. This is again most striking for the film with NiO, where $H_{c,\parallel}$ is approximately 3× larger than for the Ni/Pt sample.

M vs H for the Py films, as expected from FMR spectroscopy, shows quite different trends. As seen in Fig. 7, Py films have no easily measurable H_c using our methods, nearly full remanence, and an out-of-plane saturation field in line with that expected for the in-plane magnetic anisotropy, as dictated by the shape anisotropy of the thin film. As is the case in the Ni films, M_s is somewhat reduced from typical thin film

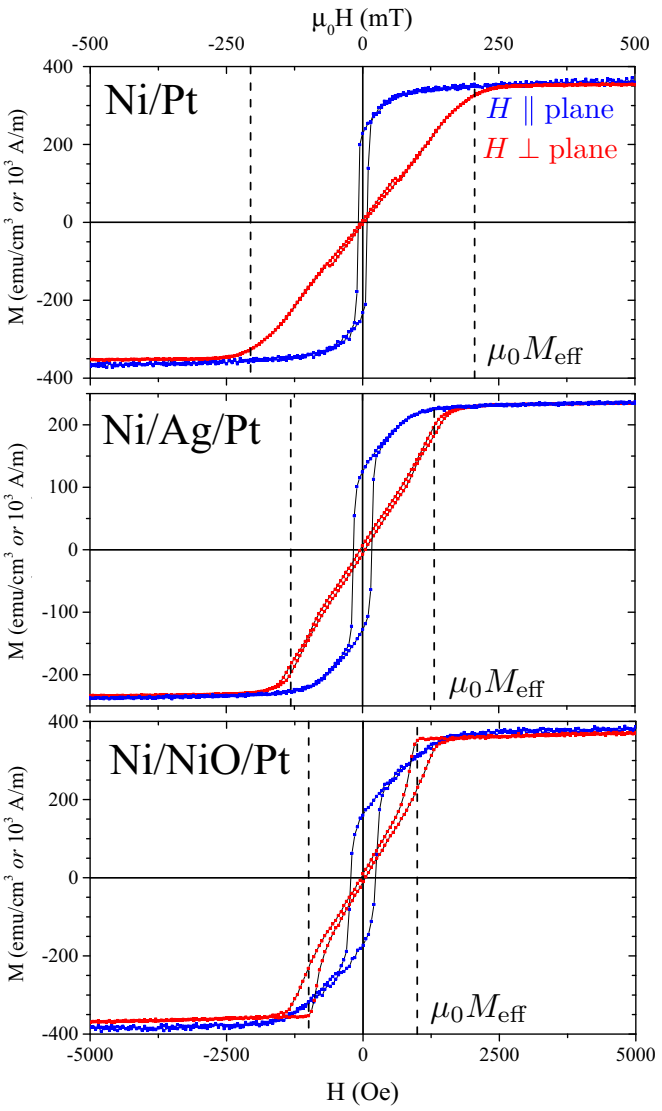

FIG. 6. In-plane and out-of-plane magnetization M vs H for Ni heterostructures at $T = 300$ K. For Ni the expected $M_s \sim 500$ emu/cm^3.

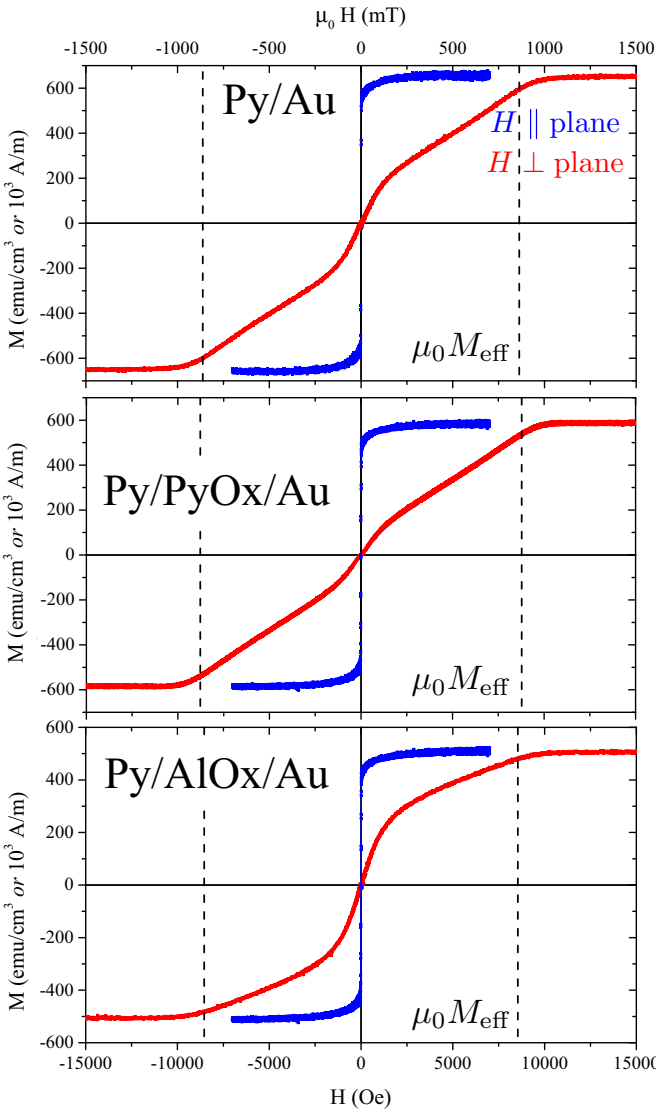

FIG. 7. In-plane and out-of-plane M vs H for Py-based heterostructures at $T = 300$ K. For Py the expected $M_s \sim 800$ emu/cm^3.

values (typically for $Ni_{80}Fe_{20}$ $M_s \approx 800$ emu/cm^3 $= 800 \times 10^3$ A/m), although similar to some previous reports [51]. The slightly Ni-rich composition of our films partially explains this, although the reduced M_s for the 85% Ni alloy is still higher than our measured values [50], which again could possibly be explained by the oxygen included in the films. The appearance of two distinct slopes in the $H \perp$ plane M in all Py heterostructures below M_s indicates an easy axis, possibly with an out-of-plane component, although the dominant anisotropy, in contrast to the Ni/Pt series, clearly remains in-plane.

Figure 8 shows the results of a detailed search for exchange bias phenomena in the Ni/NiO/Pt sample. Motivated by the M vs H loop shapes shown in Fig. 6(c), we measured M after field cooling from 300 to 10 K under an external field bias of 3000 Oe, with the sample both parallel, and then perpendicular, to the field. The resulting $H_{c\parallel}$, $H_{c\perp}$, and perpendicular exchange field, $H_{e,\perp}$, vs T are shown in Fig. 8(a), with the corresponding hysteresis loops shown in panels (b) and (c). The in-plane ($H_\parallel$) loops show that $H_{c,\parallel}$ is largest at low T, with an additional anisotropy evident in the changes in the M vs H slope below M_s that is strongly T dependent. However, no shift of the loop is measurable. This contrasts with the out-of-plane loop, which shows a similar trend in $H_{c,\perp}$ but with a significant rise near 50 K, with a clear perpendicular loop shift evident below this temperature. This confirms the presence of a perpendicular exchange bias [26] in the Ni/NiO/Pt sample with blocking temperature $T_b^{EB} = 50$ K. As shown in Fig. 8(c) the increase in H_c below T_b^{EB} is accompanied by obvious changes in $M(H)$, trending more toward perpendicular alignment. Figure 8(d) schematically depicts the structure of the rough interface region, and offers an explanation for the perpendicular anisotropy and exchange bias as discussed further below.

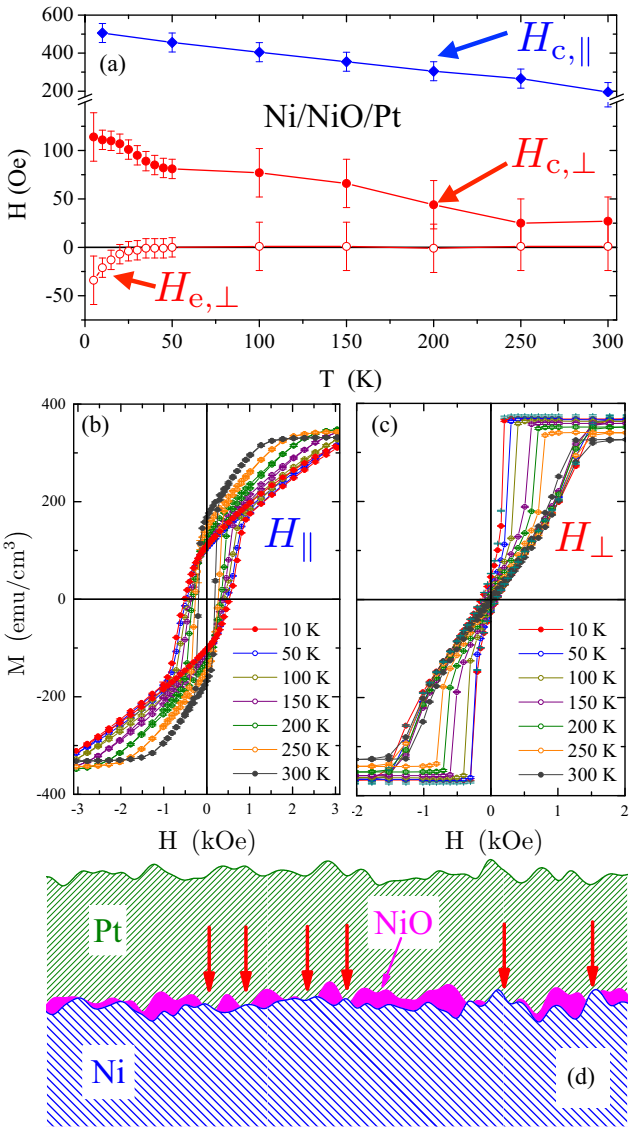

FIG. 8. Summary of evidence of perpendicular exchange bias in the Ni/NiO/Pt sample based on M measured after field cooling from 300 to 10 K under either in-plane or perpendicular external field bias of 3000 Oe. (a) Coercive field for in-plane applied field ($H_{c,\parallel}$) and out-of-plane applied field ($H_{c,\perp}$) as well as perpendicular exchange bias field ($H_{e,\perp}$) vs T. In-plane exchange bias was within error bars of $H = 0$ at all T and is not shown. (b) M vs H for in-plane applied field shown at various T. Larger field scans show a 10 K saturation near 5 kOe. (c) M vs H for out-of-plane applied field shown at various T. (d) Schematic view of the interface based on GIXR results (Fig. 2) demonstrating the proposed mechanism for EB and enhanced coercivity. Note that we have not measured the lateral length scale of the roughness, and this schematic therefore only qualitatively represents the morphology of the surfaces. Red arrows indicate points of direct Ni/Pt contact.

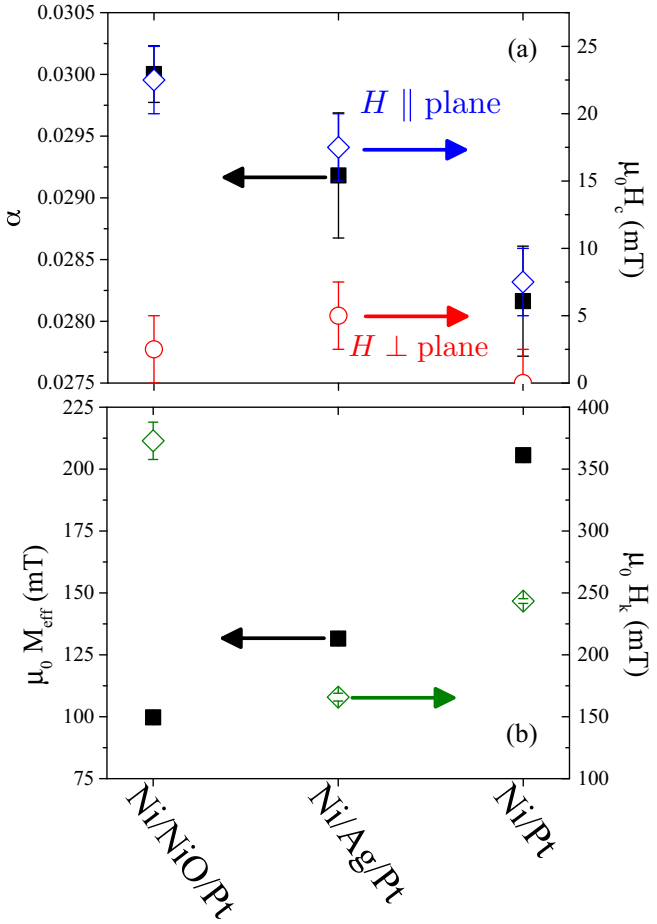

FIG. 9. Room temperature trends in (a) α (filled square), and H_c [both in-plane (open diamond) and out-of-plane (open circle)], and (b) M_{eff} (filled square) and H_k (open diamond) for the Ni/Pt sample series. Trends in α are similar to those in H_c, and suggest changes in damping are tied to magnetic anisotropy, rather than to spin pumping.

IV. DISCUSSION

A. Damping, anisotropy, and coercivity

We begin more detailed discussion of these results by comparing α and M_{eff} from broadband FMR to anisotropy fields and coercivity revealed by magnetization. Figure 9 summarizes this information for the Ni sample series. Figure 9(a) plots the damping parameter α on the left axis with H_c determined from in-plane and out-of-plane magnetization on the right axis. The damping is significantly enhanced by addition of Ag or NiO, with the oxide showing the largest effect. This trend in α clearly tracks the change in $H_{\mathbf{c},\parallel}$ observed from magnetometry. The presence of an antiferromagnetic layer in contact with a FM layer has been proven to both increase H_c and α, even at temperatures somewhat larger than T_b, the blocking temperature of the AF film [52–55]. As shown in the GIXR and AES depth profile in Figs. 2(c) and 2(d), the NiO layer is thin (and rough) with $t \approx 1.4$ nm. For this thickness, the literature suggests $T_b^{\text{EB}} < 40$ K [33,56], which could be further reduced considering the high roughness of the layer. Previous results on enhancement of H_c and α above T_b used materials with higher T_b (or T_N) so that the room temperature observation of the effect represented $T \approx 4T_b$ [53]. We have seen this effect at $T \approx 6T_b^{\text{EB}}$, suggesting that the SOC in the Pt enhances the anisotropy and exchange. The intermediate enhancement in α and H_c in the Ni/Ag/Pt sample would be surprising if a clean Ag layer is simply inserted between Ni and Pt. However, the AES depth profile for this sample [Fig. 2(f)]

showed an accumulation of both oxygen and carbon at the interface between NM and FM. This raises the possibility of partial NiO layer formation, which would explain intermediate values of α and H_c.

Figure 9(b) compares M_{eff} determined from FMR (left axis) to $H_k = M_s - M_{\text{eff}}$ again with M_s determined from in-plane SQUID magnetometry (right axis). Here we see modest positive values of H_k in Ni/Pt indicating, in agreement with the relatively easy out-of-plane saturation seen in Fig. 6, a significant out-of-plane component to the anisotropy field. The presence of the NiO layer strongly reduces M_{eff}, with a corresponding increase in H_k, and again is supported by the strongly out-of-plane anisotropy revealed in M vs H. Although the Ni/Ag/Pt sample shows intermediate M_{eff}, since M_s is lowest for this sample, H_k is smaller than in both other Ni-based samples.

This picture of the anisotropy is clarified by the perpendicular exchange bias shown in Fig. 8. Unlike the Co/Pt and Fe/Pt systems, most studies of Ni/Pt show negative (in-plane) surface anisotropies [57], and the earliest work on Ni/Pt multilayers showed perpendicular anisotropy only below 70 K [58]. Later work clarified the role of magnetocrystalline anisotropy, which can drive a given heterostructure or alloy into out-of-plane anisotropy when the film stress or other growth conditions are optimized [59–62], as well as magnetic proximity effects at the Ni/Pt interface that can induce ferromagnetism in the Pt [63]. Since we made no attempt to control the film stress in our Ni/Pt sample, we do not expect room temperature perpendicular anisotropy. However, the presence of an antiferromagnetic NiO layer on Ni is known to enhance the perpendicular anisotropy, providing a mechanism that allows such effects to persist to above room temperature [64,65]. Based on both magnetic and structural characterization of the Ni/NiO/Pt sample, we propose that the enhancement of coercivity, the presence of mixed anisotropy at room temperature that becomes increasingly perpendicular at low T, and the corresponding low-T perpendicular exchange bias are all driven by the low t_{NiO} and high interfacial roughness of this layer. This situation is shown schematically in Fig. 8(d), where the thin, rough oxide allows areas of direct contact between Ni and Pt (indicated with red arrows). These areas tend toward perpendicular anisotropy at low T, which is enhanced by the proximity to NiO or the strong SOC in Pt, or both. Note that although these areas of direct Ni/Pt contact are expected, the total area of the interface contained in such sections remains small, and does not offer a plausible explanation for the enhanced spin transport through this interface.

Turning now to the Py-based samples, Fig. 10 shows a summary of FMR properties, although here H_c, as expected, is always smaller than our field measurement uncertainty (on the order of several Oe) and we instead compare α to estimated values of effective spin-mixing conductance, $g_{\uparrow\downarrow,\text{eff}}$. We determine this entirely from FMR and magnetometry using [66]

$$g_{\uparrow\downarrow,\text{eff}} = (\alpha - \alpha_0)\frac{4\pi M_s t_{\text{F}}}{g\mu_B}. \quad (5)$$

Here α_0 is the intrinsic damping of the FM, and this equation assumes all changes in damping are due to the spin pumping. Indeed the trend in α matches the expectation for spin

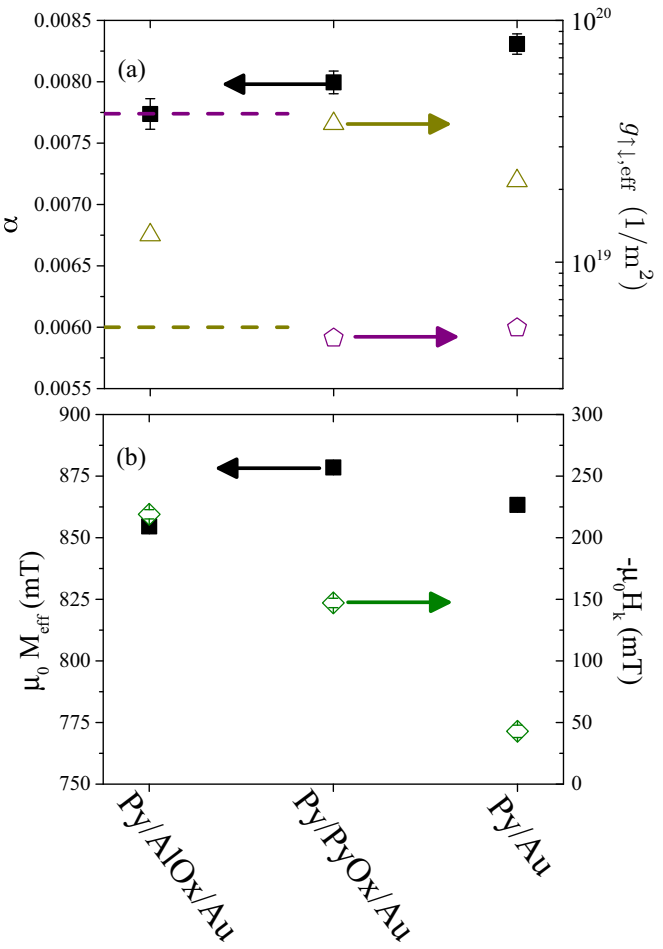

FIG. 10. Room temperature trends in (a) α (filled square), and $g_{\uparrow\downarrow,\text{eff}}$ (open triangle: for intrinsic damping = 0.006, open pentagon: for intrinsic damping = 0.0077), and (b) M_{eff} (filled square) and H_k (open diamond) for the Py/Au sample series. Trends in α here are in line with a spin-pumping origin, and we use two different estimates of intrinsic damping α_0 to estimate the spin-mixing conductance independently from the electrically detected spin-pumping measurement. These values of $g_{\uparrow\downarrow,\text{eff}}$ fall in the range expected for transition-metal FM/NM interfaces.

pumping, with the lowest value seen in the Py/AlOx/Au sample that showed the lowest dc voltage at resonance. To determine $g_{\uparrow\downarrow,\text{eff}}$ we take two different values of α_0 to estimate the full range of possible values. The largest estimate of $g_{\uparrow\downarrow,\text{eff}}$ comes from assuming the Py film has the typical intrinsic value, $\alpha = 0.006$, seen in $Ni_{80}Fe_{20}$ films [67], as indicated by the dark yellow dashed line. We estimate a lower limit by assuming that $\alpha = 0.00774$ measured for the Py/AlOx/Au film and shown as the purple dashed line is the appropriate intrinsic value for our Py films. In both cases the estimated $g_{\uparrow\downarrow,\text{eff}}$ falls in the range of typical values for FM/NM interfaces [11], and roughly indicates $g_{\uparrow\downarrow,\text{eff}} \approx 10^{19}$ 1/m^2 for the Py/Au and Py/PyOx/Au interfaces.

Fig. 10(b) compares M_{eff} determined from FMR (left axis) to $-H_k = M_s - M_{\text{eff}}$ again with M_s determined from in-plane SQUID magnetometry (right axis) for the Py heterostructures. Note the negative sign on the right axis, so that the data points represent in-plane anisotropy fields. For this series of films,

there is no strong drop in $M_{\rm eff}$, and $|H_k|$ values are small compared to the Ni series. This matches expectations from magnetometry.

V. DETERMINATION OF CONE ANGLE AND SAMPLE PARAMETERS

In electrically detected spin pumping measurements performed at fixed frequency in microwave cavities it is typical practice to use a value for the magnetization precession cone angle, Θ, estimated using the relation $\Theta = h_{\rm mw}/\Delta H$, where $h_{\rm MW}$ is the driving microwave field and ΔH is the FWHM FMR linewidth determined by fitting a Lorentzian to the measured response. Because we have measured the damping parameter, α, for this set of samples directly via broadband FMR, we can instead determine Θ more accurately from the balance between the driving microwave field and losses via damping.

In the dc electrically detected spin pumping geometry we apply a static magnetic field $\mathbf{H}_0$ along the x direction, and $h_{\rm MW}$ along the y direction. This causes the magnetization vector $\mathbf{M}$ to precess about the equilibrium direction set by $H_{\rm eff}$. The relevant components of $\mathbf{M}$ are then $M_y = m_y e^{i\omega t}$ and $M_z = m_z e^{i\omega t}$ with $m_y = \chi_{yy} h_y$ and $m_z = \chi_{zy} h_y$. χ_{yy} and χ_{zy} are elements of the Polder susceptibility tensor given by [67]

$$\chi_{yy} = \frac{\mu_0 M_{\rm s}}{D}\left[\mu_0(M_{\rm eff} + H_0) + \frac{i\omega\alpha}{\gamma}\right] \tag{6}$$

and

$$\chi_{zy} = \frac{\mu_0 M_{\rm s}}{D}\left(\frac{i\omega}{\gamma}\right), \tag{7}$$

where $\gamma = g\mu_{\rm B}/\hbar$ is the gyromagnetic ratio determined from the measured g factor, and

$$D = \left[\mu_0(M_{\rm eff} + H_0) + \frac{i\omega\alpha}{\gamma}\right]\left(\mu_0 H_0 + \frac{i\omega\alpha}{\gamma}\right) - \left(\frac{\omega}{\gamma}\right)^2. \tag{8}$$

Broadband FMR determines g, $M_{\rm eff}$, and α, which allow extraction of the cone angle of the precession that occurs in the electrically detected dc spin pumping under static field $H_0 = H_{\rm res}$ and driving field $h_y = h_{\rm MW}$. We compare $P\sin^2\Theta$ with $|m_y|\cdot|m_z|/M_s^2$ in Table I. In quantifying our results we exclusively use $|m_y|\cdot|m_z|/M_s^2$.

A. Quantification and comparison of $g_{\uparrow\downarrow,\rm eff}$ and $\alpha_{\rm SH}$

The dc voltage generated at the FM resonance via the ISHE is given [10,51] by

$$V_{\rm ISH} = \frac{e\left[\alpha_{\rm SH}\lambda_{\rm sd}\tanh\frac{t_{\rm N}}{2\lambda_{\rm sd}}\right]g_{\uparrow\downarrow,\rm eff}}{\sigma_{\rm F}t_{\rm F} + \sigma_{\rm N}t_{\rm N}}\nu_{\rm MW}LP\sin^2\Theta. \tag{9}$$

Here $\sigma_{\rm F}$ and $\sigma_{\rm N}$ are the (charge) conductivities of the FM and NM, respectively, and L is the length of the sample along the $\hat{y}$ direction as defined in Fig. 4(d). The denominator can also be written $\sigma_{\rm F}t_{\rm F} + \sigma_{\rm N}t_{\rm N} = L/(wR)$, where w is the sample width (along the $\hat{x}$ direction) and R is the measured resistance between the spin-pumping contacts. In all analysis we use this measured R, and therefore never assume any value of electrical conductivity. Backflow corrections [68] to the measured $V_{\rm ISH}$ are taken into account by using the experimentally determined $g_{\uparrow\downarrow,\rm eff}$ in place of the bare mixing conductance.

Because the parameters in this equation are all dependent on material (and in some cases thickness), for our samples we consider two regimes due to the very different $\lambda_{\rm sd}$ in Pt and Au. In the case of Pt, there has been disagreement and ongoing debate regarding the determination of $\lambda_{\rm sd}$ [7,45,69–71], with the most recent reports converging somewhat on $\lambda_{\rm sd} = 1.3$ nm [45,70]. However, nearly all reported values are $\leqslant t_{\rm Pt}$ in our heterostructures. In this first regime then $t_{\rm N} \gg \lambda_{\rm sd}$, so that $\tanh(t_n/2\lambda_{\rm sd}) \cong 1$. This gives

$$V_{\rm ISH} \cong \frac{e[\alpha_{\rm SH}\lambda_{\rm sd}]g_{\uparrow\downarrow,\rm eff}}{L/(wR)}\nu_{\rm MW}LP\sin^2\Theta \tag{10}$$

so that

$$g_{\uparrow\downarrow,\rm eff}\alpha_{\rm SH} = \frac{V_{\rm ISH}}{ewR\nu_{\rm MW}\lambda_{\rm sd}P\sin^2\Theta}. \tag{11}$$

The case of Au is different, since most sources indicate $\lambda_{\rm sd} > t_{\rm N}$. Room temperature values typically reported a range from approximately 30 to 60 nm [37,41,72]. Here we approximate by expanding $\tanh x \cong x - 1/3x^3 + \cdots$. When $\lambda_{\rm sd,Au}$ is on the order of tens of nm or more with t_n taken from GIXR (6 nm or 18 nm); this is dominated by the first term so that

$$V_{\rm ISH} \cong \frac{e[\alpha_{\rm SH}\lambda_{\rm sd}t(t_n/2\lambda_{\rm sd})]g_{\uparrow\downarrow,\rm eff}}{L/(wR)}\nu_{\rm MW}LP\sin^2\Theta \tag{12}$$

giving

$$g_{\uparrow\downarrow,\rm eff}\alpha_{\rm SH} = \frac{2V_{\rm ISH}}{ewR\nu_{\rm MW}t_{\rm n}P\sin^2\Theta}. \tag{13}$$

The values of the product $g_{\uparrow\downarrow,\rm eff}\alpha_{\rm SH}$ and $g_{\uparrow\downarrow,\rm eff}$ that result from calculations using $V_{\rm ISH}$ determined from Lorentzian fits to $V_{\rm dc}$ shown in Fig. 4 in Eqs. (11) and (13) are compared across samples in Figs. 11(a) and 11(b). In both plots the gray region indicates the range of values for $g_{\uparrow\downarrow}$ reported by Czeschka *et al.* [11]. Note that the gray region in Fig. 11(b) also corresponds well with the upper and lower limits for $g_{\uparrow\downarrow,\rm eff}$ determined for our Py samples [cf. Fig. 10(a)]. The plot of $g_{\uparrow\downarrow,\rm eff}\alpha_{\rm SH}$ confirms the two surprising results visible in the raw electrically detected spin pumping data, that the thin native oxide layers do not strongly reduce spin-pumping efficiency, and in fact enhance it by a factor of 3 for NiO and by approximately 20% for PyOx, and that Py/Au heterostructures show comparably efficient spin pumping to Ni/Pt. Our experiments cannot separately determine $g_{\uparrow\downarrow,\rm eff}$ and $\alpha_{\rm SH}$. However, for purposes of comparison to previous work we plot $g_{\uparrow\downarrow,\rm eff}$ determined using various assumed values for $\alpha_{\rm SH}$. For the Ni/Pt heterostructures, we use $\alpha_{\rm SH,Pt} = 0.11$ [13,45,70,72], which is consistent with our choice of $\lambda_{\rm SD}$ and results in $g_{\uparrow\downarrow,\rm eff}$ very much in line with expected values. Taking this approach for the Py/Au samples using the very low recently reported values for gold of only tenths of one percent or less [10,41–43], or even values $\approx$1% [44–46], requires very large $g_{\uparrow\downarrow,\rm eff}$ to explain our data. We can instead determine the $\alpha_{\rm SH}$ required to match the maximum and minimum values for $g_{\uparrow\downarrow,\rm eff}$ given by the increased damping seen in FMR [shown in Fig. 10(a)]. This requires larger values, at minimum $\alpha_{\rm SH,Au} = 0.04$, calculated assuming intrinsic damping of the Py $\alpha = 0.006$. This provides a lower limit, and larger intrinsic damping is likely in our

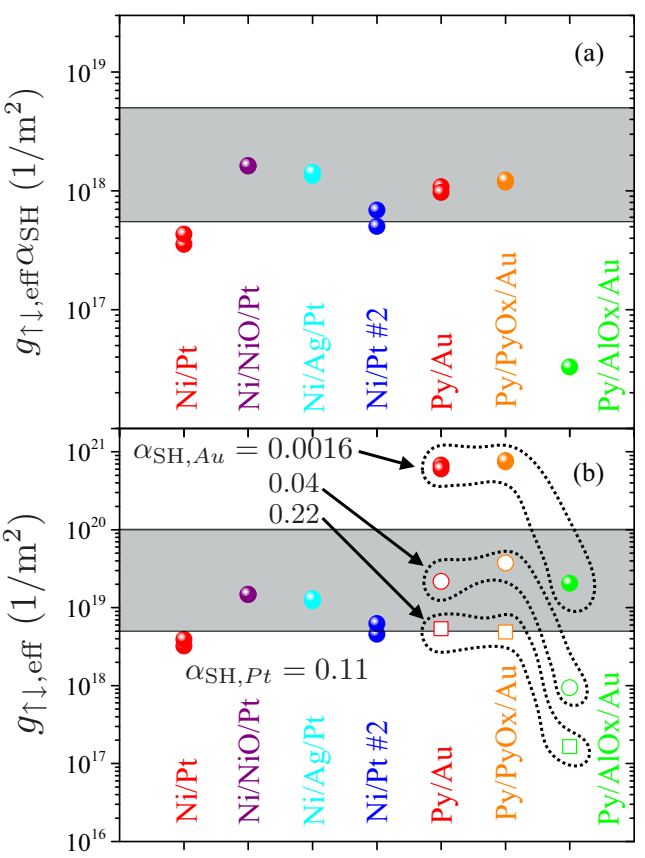

FIG. 11. (a) $g_{\uparrow\downarrow,\mathrm{eff}}\alpha_{\mathrm{SH}}$ calculated for each sample using Eq. (11) or (13). All samples show relatively similar values other than Py/AlOx/Au, which is strongly suppressed as expected. (b) $g_{\uparrow\downarrow,\mathrm{eff}}$ calculated from $g_{\uparrow\downarrow,\mathrm{eff}}\alpha_{\mathrm{SH}}$ using assumed values for α_{SH}. For Pt samples the commonly reported $\alpha_{\mathrm{SH,Pt}} = 0.11$ gives $g_{\uparrow\downarrow,\mathrm{eff}}$ in the expected range. For Au, we use three values of $\alpha_{\mathrm{SH,Au}}$. Values on the order of tenths of a percent give very large $g_{\uparrow\downarrow,\mathrm{eff}}$, even for the sample with the AlOx layer. $\alpha_{\mathrm{SH,Au}}$ of several percent or more yields $g_{\uparrow\downarrow,\mathrm{eff}}$ in line with expectations for transition-metal FM/NM interfaces.

Py films, which drives the required $\alpha_{\mathrm{SH,Au}}$ higher, with an absolute upper limit of $\alpha_{\mathrm{SH,Au}} = 0.22$ resulting from assuming identically zero spin pumping (and damping enhancement) in the Py/AlOx/Au sample. The observation of a dc voltage V_{ISH} in the Py/AlOx/Au heterostructure [cf. Fig. 4(f)] indicates the presence of a small spin current ($g_{\uparrow\downarrow,\mathrm{eff}} > 0$) such that $0.04 \leqslant \alpha_{\mathrm{SH,Au}} < 0.22$ is found. Such large spin Hall angles, reaching up to $\alpha_{\mathrm{SH,Au}} \approx 0.11$, have been previously reported in room temperature experiments on perpendicularly spin-polarized FePt/Au devices [28], as was a theoretical explanation based on a modified Kondo effect for Fe impurities in Au [31]. Both these authors and a second group [73] consider a picture where the impurity bands hybridize and lead to two Kondo resonances, one affecting transport near 1 K, and one persisting to room temperature. Measurements of nonlocal resistance in Au double-Hall bars (with no FM layers and no Fe intentionally used in the device) assumed $\lambda_{\mathrm{Au}} = 35$ nm and gave $\alpha_{\mathrm{SH,Au}}$ with an upper limit ≈0.03 [29]. This value is also on the order of the likely $\alpha_{\mathrm{SH,Au}}$ value in our heterostructures.

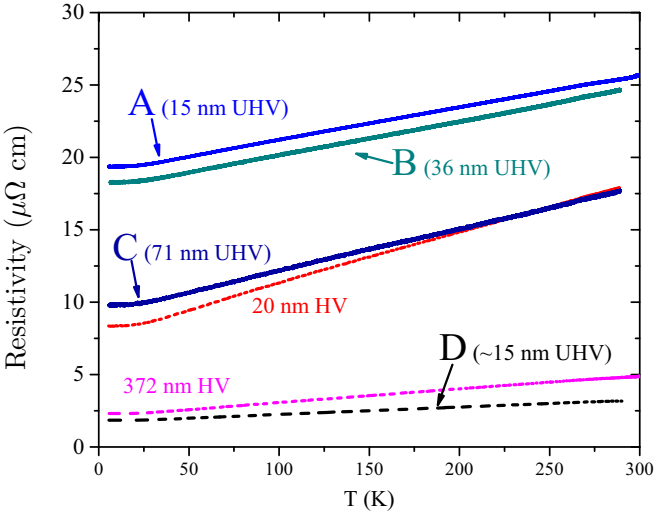

FIG. 12. Electrical resistivity vs T for Au thin films grown in the same chamber from the same source material near the time of the growth of the Au films in samples Py/Au and Py/PyOx/Au (labeled A–C) compared to other samples grown from nominally identical but uncontaminated Au source material. The very large residual resistivity indicates extensive impurities in the A–C films, likely from cross-contamination from the Py source material in the same chamber.

Although the Au films grown for this study were e-beam evaporated from nominally 99.999% pure source material in UHV, we believe a high level of magnetic impurities was unintentionally introduced to the Au source, quite likely from cross-contamination from the Py crucible used in the same system. Quantitative proof of this magnetic contamination in the actual FM/NM heterostructure is difficult due to thin layers and, of course, the presence of Ni and Fe atoms in the FM underlayer. However, indirect evidence of the contamination is shown in Fig. 12. This shows electrical resistivity for a range of evaporated Au films grown under various conditions. Films labeled "UHV" were grown via e-beam evaporation in the same chamber as the Py/Au heterostructures discussed here at base pressures $< 1 \times 10^{-8}$ Torr, while those labeled "HV" were thermally evaporated at base pressures $\sim 10^{-6}$ Torr in a chamber where magnetic metals are not deposited. The samples labeled *A*, *B*, and *C* were grown and measured sequentially on a single substrate during the time period in which the Py/Au and Py/PyOx/Au heterostructures studied in this work were grown. These three films have very high resistivity compared to typical values for these thicknesses. Film "D" was grown several months later in the same chamber after replacement of the Au crucible, and shows a much lower resistivity for the same nominal thickness as film "A." Determining impurity concentration from the residual resistivity for polycrystalline films is typically difficult or impossible since the contributions from the various defects cannot be separated. However, an extremely rough estimate of the level of impurities can be made either by determining the impurity electron mean-free path and assuming unity probability of the electron-impurity scattering or by simply comparing to literature estimates of the specific impurity resistance [74]. These suggest that Au resistivities as high

as shown here could result from between ∼500 ppm and ∼1% impurity content. The room temperature resistance measurement of the spin-pumping heterostructures (R_{SP} in Table I) provides additional evidence for high Au resistivity from impurity scattering. Estimates of resistivity for the Au layer, using the measured geometry of the heterostructure and our typical measured values of 30 $\mu\Omega$ cm for Py at room temperature, yield large values for the Au in order to explain the total resistance. Although not conclusive, this suggests that contamination of the Au layers described here is likely, and certainly argues for more thorough investigation of the effect of magnetic impurities on spin Hall angles in Au.

B. Physical origin of enhanced V_{ISH} with native oxides

Before commenting on any possible mechanism of the large V_{ISH} signals seen in the heterostructures we clarify that, as detailed in the discussion of perpendicular exchange bias above and depicted in Fig. 8(c), the thin and rough NiO and PyOx layers most likely do allow some regions of direct contact between metallic FM and NM. However we reiterate that these regions form a small fraction of the total interface area, and most likely do not play a role in the large spin pumping efficiency seen in the native oxide samples. Indeed if they are the source of the efficient spin transport between FM and NM, that transport must be much more efficient than previous measurements indicate.

Our results clearly show that the presence of thin native oxides at the interface between a metallic FM and a NM with strong SOC does not prevent the transport of spin across the interface. We note that existing studies of the native oxide of transition-metal ferromagnets are somewhat rare and have tested very different regimes that either involve long-term oxidation of the entire FM film [18] or demonstrated only a change in damping that could have other origins [19].

We restate that the enhanced V_{ISH} we have observed cannot truly separate, for example, an increase in the efficiency of the conversion between angular momentum lost at the interface into spin current injected into the NM from other mechanisms such as an increase in the effective spin-orbit coupling at the oxide-NM interface that would cause an apparent increase in α_{SH}, or an increased spin-mixing conductance. Other authors have explained similar results, including in films with similarly thin interfacial NiO layers, in terms of antiferrromagnetic magnons [21,22,75] or spin fluctuations.[21,24] Our results may support the latter, as only antiferromagnetic spin correlations, rather than true antiferromagnetic order, are present in our heterostructures at the measurement temperatures described here. Although more work is needed to clearly identify the physical mechanism that leads to the enhanced V_{ISH}, we can further consider mechanisms that could modify the spin-mixing conductance.

Enhanced spin-pumping efficiency can be driven by changes in the effective spin-mixing conductance, $g_{\uparrow\downarrow,\mathrm{eff}}$, which scales with the density of magnetic moments at a given interface [76]. So one possible explanation for the enhanced $g_{\uparrow\downarrow,\mathrm{eff}}$ in the presence of Ni (Py) oxide is an increase in the interfacial magnetization at the NiO/Pt (PyOx/Au) interface compared to the Ni/Pt (Py/Au) case. Although we know of no prior reports of direct experimental or theoretical evidence of such an enhanced interfacial moment for Ni or Py oxides, first-principles calculations do identify such an enhancement for the case of oxidized Fe surfaces [77]. This suggests that enhanced surface moments could be plausible in the case of Ni and Py, but this picture cannot entirely explain the pattern of $g_{\uparrow\downarrow,\mathrm{eff}}$ across the Ni heterostructure series apparent in Fig. 11(b). If large $g_{\uparrow\downarrow,\mathrm{eff}}$ comes from oxidized FM interfaces, one expects large values for Ni/NiO/Pt compared to both Ni/Pt *and* Ni/Ag/Pt, where the long spin diffusion length in Ag would not be expected to strongly modify the spin transport between Ni and Pt. Instead we see that Ni/Pt is indeed reduced, but Ni/NiO/Pt and Ni/Ag/Pt are large and basically equal.

An alternative scenario involving modified spin-mixing conductance offers a possible explanation for this trend in $g_{\uparrow\downarrow,\mathrm{eff}}$. In Ni/Pt heterostructures a magnetic moment is commonly induced on the Pt atoms via the magnetic proximity effect (MPE) [63]. In this case, similar to that observed where Pt is believed to be magnetized by proximity to the ferromagnet yttrium iron garnet [78], the effective interface for spin pumping becomes the FM Pt/NM Pt interface (which here will be graded and not perfectly sharp). This interface will have a different spin-mixing conductance and potentially reduced spin-pumping efficiency. The introduction of the NiO then prevents the MPE, while allowing spin transport with an overall higher effective spin-mixing conductance. This picture explains the nearly equal $g_{\uparrow\downarrow,\mathrm{eff}}$ between Ni/NiO/Pt and Ni/Ag/Pt heterostructures, since in both cases an efficient spin transport material is added between Ni/Pt, keeping the same effective spin-mixing conductance. If we also consider the Py/Au series, we see that Py/PyOx/Au and Py/Au interfaces have the same effective spin-mixing conductance. But since MPE is not observed for Au, which is far from the Stoner criterion [79], there is no FM Au/NM Au interface and no mechanism for a reduced mixing conductance, so adding the permalloy oxide simply allows spin transport from Py to Au with the same $g_{\uparrow\downarrow,\mathrm{eff}}$, as shown by the nearly equal values for these two heterostructures. Of course inserting Al_2O_3, which does not support spin transport, strongly reduces the spin pumping. Note also [Fig. 11(a)] that Ni/NiO/Pt, Ni/Ag/Pt, Py/Au, and Py/PyOx/Au heterostructures all have $g_{\uparrow\downarrow,\mathrm{eff}}\alpha_{SH}$ that agree within a factor of 2, which is consistent with the view that the moment density at the Ni/Pt and Ni-Fe/Au interfaces, and therefore the spin-mixing conductance, should be similar.

Although the presence of MPE in the Ni/Pt heterostructure helps explain the trends we have observed here, this picture still relies on efficient spin transport through oxidized Ni and Py. Although we cannot yet offer a concrete physical picture for this, our results highlight a critical need for future studies of spin transport through antiferromagnetic insulators. This work is already underway in our and other groups.

VI. CONCLUSIONS

We have presented a comprehensive set of measurements and detailed characterization to understand voltages generated by the inverse spin Hall effect in Ni and Py FM samples with Pt and Au NM layers, including those where magnetic native oxides and nonmagnetic aluminum oxides were added between the NM and FM. The presence of the oxides was confirmed by GIXR and AES analysis. We show that thin

layers of the native oxides of Ni and Py inserted between the FM and NM layers enhance the measured V_{ISH}, and in the case of NiO in proximity to Pt also lead to out-of-plane anisotropy, enhanced coercivity, and perpendicular exchange bias. We also show that the Au films used here, which likely contain some level of Fe and Ni impurities, have large spin-pumping efficiencies that are likely due to a spin Hall angle as large as $\approx$0.2, in line with the largest values reported for gold. Future work will focus both on more detailed study of α_{SH} in Au in the presence of magnetic impurities, and on more in-depth studies of damping and spin transport from transition-metal FM into NM layers via magnetic oxides.

ACKNOWLEDGMENTS

We thank A. Hojem and A. D. Avery for helpful discussions and assistance in the laboratory, J. Nogan and the IL staff at CINT for guidance and training, and T. Silva and the NIST Boulder Magnetics group for use of the FMR spectrometer, and advice and discussions of related physics. B.L.Z. and D.B. gratefully acknowledge support from the NSF (Grants No. DMR-0847796 and No. DMR-1410247). B.L.Z. also thanks the University of Minnesota Chemical Engineering and Materials Science Department, as a portion of this work benefited from support of the George T. Piercy Distinguished Visiting Professorship. Work at the University of Minnesota was supported primarily by the NSF under Grant No. DMR-1507048, with additional support from the NSF MRSEC under Grant No. DMR-1420013. The work at WMI is supported by Deutsche Forschungsgemeinschaft via SPP 1538 Spin-Caloric Transport (Project No. GO 944/4-1). Parts of this work were carried out in the Characterization Facility, University of Minnesota, which receives partial support from NSF through the MRSEC program. This work was performed, in part, at the Center for Integrated Nanotechnologies, an Office of Science User Facility operated for the US Department of Energy (DOE) Office of Science by Los Alamos National Laboratory (Contract No. DE-AC52-06NA25396) and Sandia National Laboratories (Contract No. DE-AC04-94AL85000).

[1] B. Heinrich, K. B. Urquhart, A. S. Arrott, J. F. Cochran, K. Myrtle, and S. T. Purcell, Phys. Rev. Lett. **59**, 1756 (1987).
[2] Y. Tserkovnyak, A. Brataas, and G. E. W. Bauer, Phys. Rev. Lett. **88**, 117601 (2002).
[3] Y. Tserkovnyak, A. Brataas, and G. E. W. Bauer, Phys. Rev. B **66**, 224403 (2002).
[4] M. Dyakonov and V. Perel, Phys. Lett. A **35**, 459 (1971).
[5] J. E. Hirsch, Phys. Rev. Lett. **83**, 1834 (1999).
[6] S. Zhang, Phys. Rev. Lett. **85**, 393 (2000).
[7] J. Sinova, S. O. Valenzuela, J. Wunderlich, C. H. Back, and T. Jungwirth, Rev. Mod. Phys. **87**, 1213 (2015).
[8] A. Hoffmann, IEEE Trans. Magn. **49**, 5172 (2013).
[9] E. Saitoh, M. Ueda, H. Miyajima, and G. Tatara, Appl. Phys. Lett. **88**, 182509 (2006).
[10] O. Mosendz, J. E. Pearson, F. Y. Fradin, G. E. W. Bauer, S. D. Bader, and A. Hoffmann, Phys. Rev. Lett. **104**, 046601 (2010).
[11] F. D. Czeschka, L. Dreher, M. S. Brandt, M. Weiler, M. Althammer, I.-M. Imort, G. Reiss, A. Thomas, W. Schoch, W. Limmer, H. Huebl, R. Gross, and S. T. B. Goennenwein, Phys. Rev. Lett. **107**, 046601 (2011).
[12] J. Slonczewski, J. Magn. Magn. Mater. **159**, L1 (1996).
[13] M. Weiler, M. Althammer, M. Schreier, J. Lotze, M. Pernpeintner, S. Meyer, H. Huebl, R. Gross, A. Kamra, J. Xiao, Y.-T. Chen, H. J. Jiao, G. E. W. Bauer, and S. T. B. Goennenwein, Phys. Rev. Lett. **111**, 176601 (2013).
[14] V. Castel, N. Vlietstra, B. J. van Wees, and J. B. Youssef, Phys. Rev. B **86**, 134419 (2012).
[15] C. W. Sandweg, Y. Kajiwara, A. V. Chumak, A. A. Serga, V. I. Vasyuchka, M. B. Jungfleisch, E. Saitoh, and B. Hillebrands, Phys. Rev. Lett. **106**, 216601 (2011).
[16] B. Heinrich, C. Burrowes, E. Montoya, B. Kardasz, E. Girt, Y.-Y. Song, Y. Sun, and M. Wu, Phys. Rev. Lett. **107**, 066604 (2011).
[17] B. F. Miao, S. Y. Huang, D. Qu, and C. L. Chien, Phys. Rev. Lett. **112**, 236601 (2014).
[18] S.-I. Kim, M.-S. Seo, J.-H. Seo, H. J. Yun, J. Lee, Y. S. Choi, and S. Young Park, Curr. Appl. Phys. **14**, 1743 (2014).
[19] D.-H. Kim, H.-H. Kim, and C.-Y. You, Appl. Phys. Lett. **99**, 072502 (2011).
[20] O. Mosendz, J. E. Pearson, F. Y. Fradin, S. D. Bader, and A. Hoffmann, Appl. Phys. Lett. **96**, 022502 (2010).
[21] H. Wang, C. Du, P. C. Hammel, and F. Yang, Phys. Rev. Lett. **113**, 097202 (2014).
[22] C. Hahn, G. de Loubens, V. V. Naletov, J. B. Youssef, O. Klein, and M. Viret, Europhys. Lett. **108**, 57005 (2014).
[23] R. Cheng, J. Xiao, Q. Niu, and A. Brataas, Phys. Rev. Lett. **113**, 057601 (2014).
[24] Y. Shiomi and E. Saitoh, Phys. Rev. Lett. **113**, 266602 (2014).
[25] A. Brataas, Y. V. Nazarov, and G. E. W. Bauer, Phys. Rev. Lett. **84**, 2481 (2000).
[26] S. Maat, K. Takano, S. S. P. Parkin, and E. E. Fullerton, Phys. Rev. Lett. **87**, 087202 (2001).
[27] S. M. Zhou, L. Sun, P. C. Searson, and C. L. Chien, Phys. Rev. B **69**, 024408 (2004).
[28] T. Seki, Y. Hasegawa, S. Mitani, S. Takahashi, H. Imamura, S. Maekawa, J. Nitta, and K. Takanashi, Nat. Mater. **7**, 125 (2008).
[29] G. Mihajlović, J. E. Pearson, M. A. Garcia, S. D. Bader, and A. Hoffmann, Phys. Rev. Lett. **103**, 166601 (2009).
[30] H. L. Wang, C. H. Du, Y. Pu, R. Adur, P. C. Hammel, and F. Y. Yang, Phys. Rev. Lett. **112**, 197201 (2014).
[31] G.-Y. Guo, S. Maekawa, and N. Nagaosa, Phys. Rev. Lett. **102**, 036401 (2009).
[32] J. M. D. Coey, *Magnetism and Magnetic Materials* (Cambridge University Press, Cambridge, 2009).
[33] X. Y. Lang, W. T. Zheng, and Q. Jiang, Nanotechnology **18**, 155701 (2007).
[34] On very close inspection of the O background in the Ni/NiO/Pt heterostructure, one is tempted to conclude that the background O signal found through the bulk of the Ni (and certainly added during growth due to the relatively poor HV conditions) for this heterostructure is lower than for the other two Ni samples. However, the difference is only $\sim$5% at best, and this is within the meaningful accuracy of the sensitivity corrections made to

the Auger detector response and cross section, which are on the order of 5%–10% unless a direct calibration against a separate measurement can be made. Since this is not straightforward for these heterostructures, we emphasize that the relative shape of the O signal (showing accumulation at the interface where oxidation was allowed) is the most significant conclusion from the O Auger peak.

[35] G. Mihajlovic, D. K. Schreiber, Y. Liu, J. E. Pearson, S. D. Bader, A. K. Petford-Long, and A. Hoffmann, Appl. Phys. Lett. **97**, 112502 (2010).

[36] M. R. Fitzsimmons, T. J. Silva, and T. M. Crawford, Phys. Rev. B **73**, 014420 (2006).

[37] J. Bass and W. P. Pratt, J. Phys.: Condens. Matter **19**, 183201 (2007).

[38] K. O'Grady, S. Greaves, and S. Thompson, J. Magn. Magn. Mater. **156**, 253 (1996).

[39] S. H. Charap and E. Fulcomer, J. Appl. Phys. **42**, 1426 (1971).

[40] S. B. Bailey, T. M. Peterlin, R. T. Richard, and E. N. Mitchell, J. Appl. Phys. **41**, 194 (1970).

[41] M. Isasa, E. Villamor, L. E. Hueso, M. Gradhand, and F. Casanova, Phys. Rev. B **91**, 024402 (2015).

[42] D. Qu, S. Y. Huang, B. F. Miao, S. X. Huang, and C. L. Chien, Phys. Rev. B **89**, 140407 (2014).

[43] V. Vlaminck, J. E. Pearson, S. D. Bader, and A. Hoffmann, Phys. Rev. B **88**, 064414 (2013).

[44] Y. Niimi, H. Suzuki, Y. Kawanishi, Y. Omori, T. Valet, A. Fert, and Y. Otani, Phys. Rev. B **89**, 054401 (2014).

[45] M. Obstbaum, M. Härtinger, H. G. Bauer, T. Meier, F. Swientek, C. H. Back, and G. Woltersdorf, Phys. Rev. B **89**, 060407 (2014).

[46] H. Y. Hung, G. Y. Luo, Y. C. Chiu, P. Chang, W. C. Lee, J. G. Lin, S. F. Lee, M. Hong, and J. Kwo, J. Appl. Phys. **113**, 17C507 (2013).

[47] L. Bai, Z. Feng, P. Hyde, H. F. Ding, and C.-M. Hu, Appl. Phys. Lett. **102**, 242402 (2013).

[48] J. M. Shaw, H. T. Nembach, T. J. Silva, and C. T. Boone, J. Appl. Phys. **114**, 243906 (2013).

[49] H. T. Nembach, T. J. Silva, J. M. Shaw, M. L. Schneider, M. J. Carey, S. Maat, and J. R. Childress, Phys. Rev. B **84**, 054424 (2011).

[50] R. C. O'Handley, *Modern Magnetic Materials: Principles and Applications* (John Wiley and Sons, Inc., Hoboken, NJ, USA, 2000).

[51] O. Mosendz, V. Vlaminck, J. E. Pearson, F. Y. Fradin, G. E. W. Bauer, S. D. Bader, and A. Hoffmann, Phys. Rev. B **82**, 214403 (2010).

[52] M. J. Pechan, D. Bennett, N. Teng, C. Leighton, J. Nogués, and I. K. Schuller, Phys. Rev. B **65**, 064410 (2002).

[53] C. Leighton, H. Suhl, M. J. Pechan, R. Compton, J. Nogués, and I. K. Schuller, J. Appl. Phys. **92**, 1483 (2002).

[54] M. Grimsditch, A. Hoffmann, P. Vavassori, H. Shi, and D. Lederman, Phys. Rev. Lett. **90**, 257201 (2003).

[55] E. Shipton, K. Chan, T. Hauet, O. Hellwig, and E. E. Fullerton, Appl. Phys. Lett. **95**, 132509 (2009).

[56] M. Gruyters, J. Magn. Magn. Mater. **248**, 248 (2002).

[57] M. T. Johnson, P. J. H. Bloemen, F. J. A. den Broeder, and J. J. de Vries, Rep. Prog. Phys. **59**, 1409 (1996).

[58] R. Krishnan, H. Lassri, M. Porte, M. Tessier, and P. Renaudin, Appl. Phys. Lett. **59**, 3649 (1991).

[59] Y.-S. Kim and S.-C. Shin, Phys. Rev. B **59**, R6597 (1999).

[60] G. Srinivas and S.-C. Shin, J. Magn. Magn. Mater. **198–199**, 341 (1999).

[61] S.-C. Shin, G. Srinivas, Y.-S. Kim, and M.-G. Kim, Appl. Phys. Lett. **73**, 393 (1998).

[62] D. Vasumathi, A. Shapiro, B. Maranville, and F. Hellman, J. Magn. Magn. Mater. **223**, 221 (2001).

[63] F. Wilhelm, P. Poulopoulos, G. Ceballos, H. Wende, K. Baberschke, P. Srivastava, D. Benea, H. Ebert, M. Angelakeris, N. K. Flevaris, D. Niarchos, A. Rogalev, and N. B. Brookes, Phys. Rev. Lett. **85**, 413 (2000).

[64] W. Pan, Y.-T. Shih, K.-L. Lee, W.-H. Shen, C.-W. Tsai, D.-H. Wei, Y.-L. Chan, and H.-C. Chang, J. Appl. Phys. **111**, 07C113 (2012).

[65] R. Shan, J. Du, X. X. Zhang, L. Sun, W. W. Lin, H. Sang, T. R. Gao, and S. M. Zhou, Appl. Phys. Lett. **87**, 102508 (2005).

[66] Y. Tserkovnyak, A. Brataas, G. E. W. Bauer, and B. I. Halperin, Rev. Mod. Phys. **77**, 1375 (2005).

[67] M. Weiler, J. M. Shaw, H. T. Nembach, and T. J. Silva, Phys. Rev. Lett. **113**, 157204 (2014).

[68] H. J. Jiao and G. E. W. Bauer, Phys. Rev. Lett. **110**, 217602 (2013).

[69] J.-C. Rojas-Sánchez, N. Reyren, P. Laczkowski, W. Savero, J.-P. Attané, C. Deranlot, M. Jamet, J.-M. George, L. Vila, and H. Jaffrès, Phys. Rev. Lett. **112**, 106602 (2014).

[70] L. Liu, R. A. Buhrman, and D. Ralph, arXiv:1111.3702.

[71] L. Vila, T. Kimura, and Y. C. Otani, Phys. Rev. Lett. **99**, 226604 (2007).

[72] M. Althammer, S. Meyer, H. Nakayama, M. Schreier, S. Altmannshofer, M. Weiler, H. Huebl, S. Geprägs, M. Opel, R. Gross, D. Meier, C. Klewe, T. Kuschel, J.-M. Schmalhorst, G. Reiss, L. Shen, A. Gupta, Y.-T. Chen, G. E. W. Bauer, E. Saitoh, and S. T. B. Goennenwein, Phys. Rev. B **87**, 224401 (2013).

[73] T. A. Costi, L. Bergqvist, A. Weichselbaum, J. von Delft, T. Micklitz, A. Rosch, P. Mavropoulos, P. H. Dederichs, F. Mallet, L. Saminadayar, and C. Bäuerle, Phys. Rev. Lett. **102**, 056802 (2009).

[74] R. Berman and J. Kopp, J. Phys. F **1**, 457 (1971).

[75] R. Khymyn, I. Lisenkov, V. S. Tiberkevich, A. N. Slavin, and B. A. Ivanov, arXiv:1511.05785.

[76] X. Jia, K. Liu, K. Xia, and G. E. W. Bauer, Europhys. Lett. **96**, 17005 (2011).

[77] H. W. Hugosson, W. Cao, S. Seetharaman, and A. Delin, J. Phys. Chem. C **117**, 6161 (2013).

[78] Y. Sun, H. Chang, M. Kabatek, Y.-Y. Song, Z. Wang, M. Jantz, W. Schneider, M. Wu, E. Montoya, B. Kardasz, B. Heinrich, S. G. E. te Velthuis, H. Schultheiss, and A. Hoffmann, Phys. Rev. Lett. **111**, 106601 (2013).

[79] D. Qu, S. Y. Huang, J. Hu, R. Wu, and C. L. Chien, Phys. Rev. Lett. **110**, 067206 (2013).